1-1-2013

Fundamental Studies And Applications Of Strong Field Ionization

Lu Yan
Wayne State University,

FUNDAMENTAL STUDIES AND APPLICATIONS OF STRONG FIELD IONIZATION

by

LU YAN

DISSERTATION

Submitted to the Graduate School

of Wayne State University,

Detroit, Michigan

in partial fulfillment of the requirements

for the degree of

DOCTOR OF PHILOSOPHY

2013

MAJOR: CHEMISTRY (Physical)

Approved by:

_____

Advisor Date

_____

_____

_____

_____

DEDICATION

This dissertation is dedicated to

my father: Yan, Fei;

my brother: Wang, Ying;

my husband: Shen, Lei.

ACKNOWLEDGMENTS

First of all, I would like to thank my advisor Prof. Arthur Suits, who allowed me to join his group and spend my graduated school years with wonderful Suits group members.

I worked with Nuradhika at first for some photodissociation experiments. She taught me how to operate the laser as well as some fundamental knowledge of the apparatus and helped me a lot when I was a beginner in the lab. She is a sister to me in this group with some special help in various ways.

Life changed a lot in summer 2010 due to the change of research project. I joined the strong field DC sliced imaging project with Prof. Suits help. During this period, I worked with Prof. Suits and he was very patient to explain the theory, and help me to work on the experiment. Prof. Wen Li also helped me a lot when I was working on this project. He was very experienced on the femtosecond chemistry and knowledgable of the operation of the femtosecond laser. I appreciate them for all kinds of help during my PhD life. Fadia joined this project in my last year and she was a very nice girl to help me in various ways not only for the experiment.

Thanks for all the former and current group members: Dr. Estillore, Dr. Wilson Gichuhi, Dr. Nuradhika Herath, Dr. Ruchira Silva, Bernadette Broderick, Chamara Abeysekera, Yuanyuan Shi, Richard Van Camp, Ravin Fernando, Michael B. Doyle, Dr. Joalland Baptiste, Dr. James Oldham and Dr. Prashant Chandra Singh, Yunmin Lee. The atmosphere of this lab is happy with

friendship and teamwork with so many ideas.

I also need to thank the group members in Li group: Dr. Sue Kyoung Lee, Yunfei Lin, Thushani Herath and Alex Winney for their help of my experiments related to the femtosecond project. I thank the members of my dissertation committee: Prof. Wen Li, Prof. Sarah Trimpin and Prof. Jogindra Mohan Wadehra for their help and suggestion of the prospectus and this dissertation. For the staff of the Chemistry Department for helping during my phd studies, I thank Melissa Barton, Erin Bachert, Deborah McCreless, Diane Kudla, Nester Ocampo and Marry wood. Thanks all my friends in the Chemistry Department, Bo Yang , Ranran Wu et al. for help when I was homesick.

Finally, I want to acknowledgment my family members, my parents and my husband Dr. Lei Shen. Without their help, it would be impossible for me to do the Phd. work in these five years. They were persons for me to talk with when I was temporarily negative with my life. They supported me strongly to continue this PhD life.

Thanks my husband who took the flight so many times to visit me and to support me when we were in long distance even in busy work.

In summary, thanks all the people who helped me in these five years in various ways.

TABLE OF CONTENTS

LIST OF TABLES

LIST OF FIGURES

Chapter 1

INTRODUCTION OF STRONG FIELD IONIZATION OF ATOMS AND MOLECULES

1.1 Strong field ionization

In an intense, infrared or near-infrared laser field, the mechanism of ionization of atoms and molecules is different from that in low-intensity fields. In low-intensity fields, the atoms and molecules require photons with enough energy to be directly ionized via resonance to a certain electronic state with the ionization later or continuum directly. However, in an intense laser field, resonance ionization is not necessary even for photons with less photon energy limit. The atoms and molecules will experience nonresonant ionization with more photons in the laser field, like nonresonant multiphoton ionization or tunneling ionization.

When an electron is in an electric field, the averaged energy of the electron can be given by the ponderomotive potential given by the equation below (Eq (1.1)):

$$U_p = \frac{e^2 E_0^2}{4m\omega^2} = 9.33 \times 10^{-14} I_0 \lambda^2 (eV) \tag{1.1}$$

where $I_0(W/cm^2)$ is the laser intensity, E_0 is the electric field strength and λ is the

wavelength of the laser. With a typical Ti:sapphire laser output at ~800 nm, when its pulse intensity is $\sim 10^{14} W/cm^2$, the ponderomotive potential will reach to several electron volts. If the ponderomotive potential is comparable with the ionization potential (I_p) of the atoms or molecules, the tunneling ionization regime (Fig. 1.1(c)) can compete with the nonresonant multiphoton ionization regime (Fig. 1.1(b)).

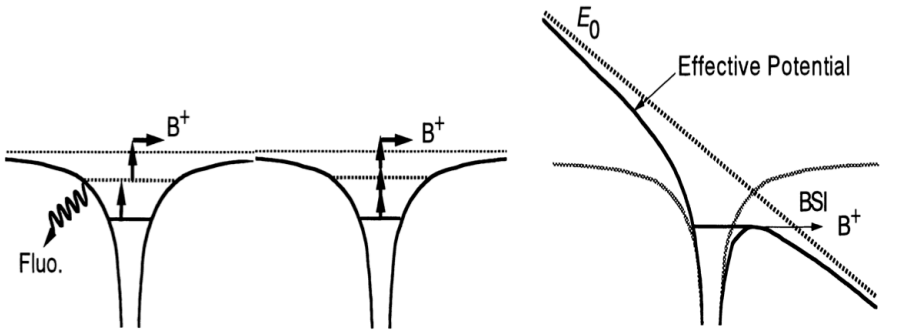

Figure 1.1: A representation of (a) REMPI and LIF. (b) Nonresonant multiphoton ionization. (c) Tunneling ionization (Adapted from Nakashima et al.[52])

The ionization regimes in an oscillate laser field can be classified by the Keldysh parameter[40] $\gamma = (I_p/2U_p)^{1/2}$. If $\gamma \gg 1$, the ionization prefers the multiphoton regime. If $\gamma \ll 1$, the strong laser field suppresses the potential barrier (Coulomb potential) and the optical frequency of the field is low enough, so the electron has the time to tunnel out of the potential barrier to the continuum (Fig 1.1). The ionization preferes tunneling regime.

1.2 Ionization of atoms and molecules in an intense laser field

In an intense laser field, the tunneling ionization of atoms and molecules has been interpreted by several models, such as the Ammosov-Delone-Krainov (ADK)[1] model, the barrier suppression ionization (BSI)[2] model and the Keldysh-Faisal-Reiss (KFR)[5] model. The ADK theory is based on the 3-dimensional (3D) tunneling ionization model. It predicts that the ionization rate depends on the ionization potential of the neutral atoms in an external static electric field. It extends a hydrogenlike atom to a complex atom by a quasiclassical approximation and it successfully predicts the ionization rate of rare gas atoms. The BSI model describes that the external field suppresses the Coulomb potential, which results in a lower barrier through which the electron can decay when the threshold is reached. The KFR model is based on scattering theory and involves a transition from an initial state of the target to the final state in an electric field.

With molecules, these theories cannot provide a good prediction of their ionization rate in an intense laser field. This is because the ionization may compete with molecular decomposition. Furthermore, at higher laser intensity, Coulomb explosion may happen and induce multicharged ions and fragments.

The BSI model was furthur developed by Corkum et al.[24] who focused on the molecular ion yield and how it varies with the laser peak intensity. They concluded that the ion signals was proportional to the logarithm of the peak laser intensity (Eq(1.2))[24] by using sudden approximation[2] to describe the simple BSI model in a cylindrical geometry.

$$S = \alpha\pi R^2 cl\phi[ln(I_0) + ln(I_{sat})] \tag{1.2}$$

where α is the instrument sensitivity, R is the Rayleigh length of the focused laser beam, c is the concentration of the atoms or molecules, l is the length of the cylinder (i.e. time-of-flying tube) projected on the detector, ϕ is the ionization branching ratio which is independent with the laser peak intensity, I_0 is the peak laser intensity and I_{sat} is the saturation intensity of the molecules or atoms. For rare gas atoms, $\phi = 1$ and $\phi \leq 1$ for molecules due to the fragmentation. With the sudden approximation, when $I_0 > I_{sat}$, the ionization rate goes to infinity and if $I_0 < I_{sat}$ the ionization rate is zero. Therefore, the saturation intensity (I_{sat}) indicates the threshold just needed by the electron to escape from the atom or the molecule. Recently, Dantus et al.[47] found there was intense signal-to-noise level above I_{sat} of organic molecules in SFI by using a femtosecond laser. The fragmentation partern of a certain molecules only depends on the averaged laser pulse duration and it is not related to the laser pulse shape. Harada et al. also concluded that if there was an overlap between the molecule radical ion absorption spectra and the ionization laser wavelength (i.e. 800nm for Ti:sapphire fundamental femtosecond laser), the molecule could experience more fragmentation. The distinct fragmentation og various molecules provides a potential of using femtosecond laser as an ionization source of mass spectrometer. The details about mass spectrometry using femtosecond laser will be discussed in Chapter 4 in details.

1.3 Introduction to each chapter

The thesis is organized as follows:

Chapter 2 introduces a new ion imaging technique which can achieve near universal detection of photofragments in the photodissociation process. The details of this strong field DC sliced "raster" imaging is introduced followed with the apparatus and

some samples examined. By replacing the probe laser used to ionize the photofragments with a femtosecond laser, a wider range of photofragments can be detected compared with the resonant multiphoton ionization. We examine the photodissociation of sulfur dioxide and nitromethane at 193 nm by obtaining the images of SO from SO_2 and methyl radical, NO and O from nitromethane. The SO fragment detection is used as a calibration of the apparatus and the mechanism of photodissociation of nitromethane is discussed compared with some investigation via other techniques.

The strong field ionization sensitivity of nonstatistical magnetic quantum numbers is investigated in Chapter 3. By measuring the argon double cation yield from the sequential double ionization, we show that the ionization yield is sensitive to the sign of the magnetic quantum number. The laser beam is split to pump and probe beams with both circularly polarized. The pump beam ionizes the argon neutral atoms to single cation at first and then the probe beam ionizes the argon single cation to argon double cation. This is a sequential double ionization process. The difference of the argon double cation yield between the same and opposite helicites of the pump and probe light is $\sim 300\%$ by experimental measurements, which is in fair agreement with the theoretical prediction. We conclude that in the circularly polarized light field, the atoms show ionization rate that depends on the sign of the magnetic quantum number of the argon subshell electrons. However, this is a qualitative investigation with as yet unknown sign of magnetic quantum number influencing the ionization rate. More experiments with known orientated atoms product produced should be investigated in the future.

In chapter 4, a "semi-soft" ionization via strong field ionization is used to identify and classify the component of complex mixture, including isomeric identity. An femtosecond laser source is utilized as an ionization source of a time-of-flight mass spectrometer. In an intense ultrashort pulsed laser field, some molecules undergo

moderate fragmentation, some just minimal fragmentation. This character of the molecules in strong field is applied to specify the isomers via the characteristic fragmentation of different isomers. The mass spectrum of each isomer are treated as "basis functions" to identify the concentration of them in a complex mixture quantitatively by a simple linear combination method. Several pairs of the isomers are examined.

Chapter 2

STRONG FIELD DC SLICE IMAGING

2.1 DC Slice raster imaging

2.1.1 Introduction of velocity map imaging (VMI)

The ion-imaging technique was first introduced by Chandler and Houston[12] in 1987 with state-resolutive image of the velocity distribution of methyl radicals from the photodissociation of methyl iodide. One of the advantages of the ion-imaging technique compared with Doppler probing[36, 76] and other techniques is that it is a straight forward way to obtain the translational energy distribution and angular distribution simultaneously from the photodissociation process. In their design, the molecular beam was introduced into the main chamber by a pulsed valve coupled with a skimmer. The parent molecules were dissociated by a photolysis laser on the axis of a TOF mass spectrometer. They installed a pair of grids in front of the ion detector. The ions created by the photolysis laser were accelerated through time-of-flight mass spectrometer. During the flying, the ion cloud expanded and impinged onto the surface of a two-dimensional (2D) position-sensitive detector (microchannel plate (MCP)) coupled with a phosphor screen. The image signal on the phosphor screen was recorded by either polaroid film or a two-dimentional intensified reticon

array .

This setup has been widely adapted worldwide as a general design for ion imaging, however the potential of its application was hindered by its low resolution until the innovation of velocity map imaging (VMI) technique by Eppink and Parker in 1997[21]. They removed the pair of grids from the electrodes and the ion optics acted as electrostatic lenses to focus the ions sharply onto the ion detector. The ions with the same initial recoil velocity were focused onto the same spot of the detector regardless of the initial location in the interaction region. As a result, the resolution of the image was improved dramatically. The ion images obtained from VMI were still in 2D distribution with the ions detected by MCP. A mathematical transformation, such as the inverse Abel transformation was necessary to reconstruct the 3D distribution from 2D images[29]. This always introduced some artificial noise into the transformed images, especially along the laser polarization axis. Another limitation was that the fragment distribution must be cylindrically symmetric with respect to an axis parallel to the plane of the imaging detector. However, in some cases of two-color experiments, some special laser polarization alignments for pump and probe lasers are needed.

2.1.2 Strong field direct current (SFDC) slice imaging as "raster" imaging

Another technique, termed DC slice imaging[69] was developed in our group. In this appratus, the central slice of the ion cloud is detected to obtain the 3D distribution directly. By inserting an additional lens in the ion optics, the ion cloud is stretched more with relatively lower voltage of the repeller, which is expanded enough "gate" the MCP detector to sample the central slice from which the 3D distribution

is directly obtained. The photolysis laser and the probe laser are overlapped and interact with the molecular beam. The parent molecules are dissociated and the fragments are ionized at the same position in this geometry.

If the probe laser is not overlapped with the pump laser, it can be offset from the pump laser to achieve "raster" imaging. In this geometry, the probe laser is set the downstream of the photolysis interaction area with a certain time delay after the photodissociation event. By slowly moving the probe laser perpendicularly to the flight axis (Fig. 2.1), there should be an effective ionization volume which only depends on the laser focusing volume. If there is an appropriate distance and time delay between the photolysis event and ionization by the probe laser, the probe laser can selectively ionize the central slice of the fragment cloud. With only the ions from the central slice detected by the MCP, therefore, it is not necessary to apply the narrow time "gate" on the MCP because the probe laser slices the neutral fragment cloud which is unrelated to the timing of the detector.

Traditionally, the probe laser source is employed to ionize the neutral fragments by using resonance enhanced multiphoton ionization (REMPI). It can be accessible easily by visible dye laser light with frequency doubling/tripling. For (N+M) REMPI, the fragment absorbs N photons simultaneously if the sum of the energy of the N photons equal the energy gap between the ground state and a excited state. Then, the fragment can be ionized by the absorption of additional M photons. In photodissociation dynamics, state-selective probe of some photofragments can be achieved by REMPI, especially for some atomic and diatomic fragments.

Many photofragments do not process effective REMPI detection. However, it is possible to ionize them by a femtosecond(fs) laser with short pulses by strong field ionization. The photofragments generated from the photodissociation process can be ionized in an intense laser field via tunneling, with the femtosecond laser as a probe

laser. When the laser intensity is strong enough and above the saturation intensity of a certain photofragment, all the photofragments in the laser focal region should be ionized (sudden model[2]). The key factor of fragmentation in strong field ionization is whether the absorption resonances of the cations are overlapped with the fs laser wavelength[27] (all considered here will be Ti-sapphire fundamental, $\sim 780-820$ nm). Fortunately, this implies that for detection of radicals produced by photodissociation, for which the cations are closed-shell, little fragmentation will be the general rule.

In our experiments, we implement strong field ionization and DC sliced "raster" imaging together by using a femtosecond laser (Ti-sapphire 800 nm) as a probe laser to achieve universal detection of ion imaging and explore the detailed dynamics of polyatomic molecules. We detected the photofragments from the dissociation of sulfur dioxide and nitromethane via strong field "raster" imaging. The details of the experimental setup and laser alignment are discussed in the next section.

2.2 Experimental Setup

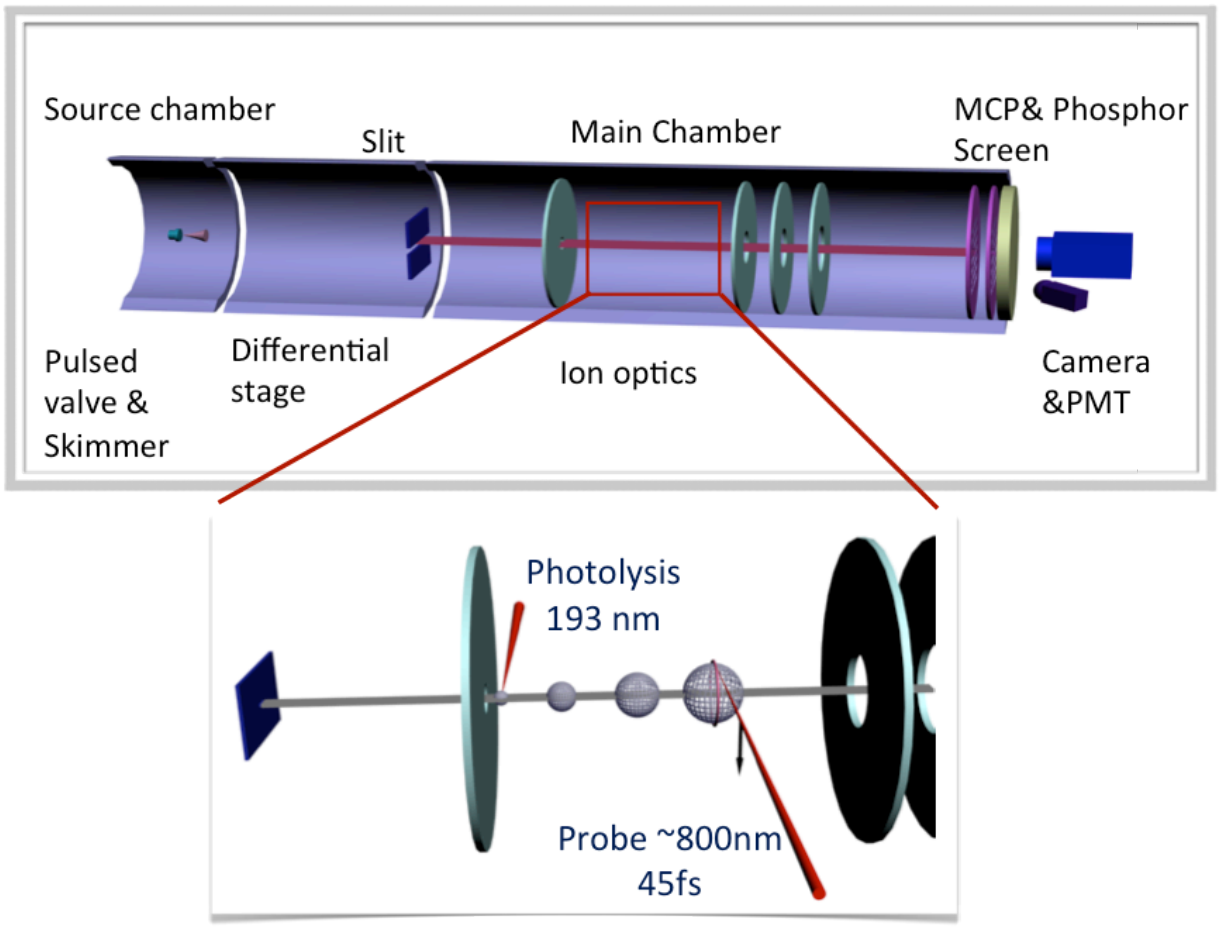

Figure 2.1: Schematic diagram of experiment setup for strong field DC slice raster imaging

The overall experimental setup for strong field DC slice raster imaging with vacuum system and laser sources is shown schematically in Fig.2.1. The apparatus is pumped separately by different turbo molecular pumps for source chamber, differential stage and main chamber. With the differential stage reducing the pressure in the main chamber, the background signal from the ionization in main chamber can be further reduced. In normal operation, the pressure of source chamber and main chamber was $\sim 10^{-6} torr$ and $\sim 10^{-9} torr$, respectively. A gas sample seeded

in helium was introduced via a piezo valve and nozzle (1 mm) operating at 100 Hz with backing pressure of 1 bar. The pressure was $\sim 10^{-5}$ torr and $\sim 10^{-8}$ torr in the source and main chambers with the molecular beam turned on, respectively. After passing through a skimmer, the molecular beam entered the differential stage and then arrived the region of main chamber via a slit between the differential stage and main chamber. This slit could reduce the number density of molecular beam in reaction area between repeller and extractor to avoid strong space charge effect. There were additional two lenses behind the extractor in the ion optics part to stretch ion cloud. The molecular beam was intersected at a right angle by laser beams. An excimer laser (ArF, 100Hz, EX10, GAM Laser. Inc.) operated at 193 nm was utilized as a photolysis laser with a ∼40 cm focal length lens. The photolysis laser beam was loosely focused to molecular beam with the distance between the focus lens and beam around 30 cm to assure a large photodissociation volume. The probe laser was provided by a near infrared femtosecond Ti:Sapphire amplified laser system (800 nm, ∼70 fs, 1 kHz, KMlabs, Wyvern 1000) with 40 cm focusing. The power of the probe laser was adjusted manually by several neutral density filters set in front of the focus lens with pure horizontally polarization. To do the "raster" imaging, the time delay between the photolysis and probe laser beams was several microseconds. As a result, with enough expansion of the fragment cloud, the probe beam could be focused on the central slice of the ion fragments. The focus lens of the probe beam was placed on a translational stage in order to be moved vertically to scan the photofragment cloud. After passing through a 1 m field free flight tube, the ions were detected by using a dual MCP/phosphor screen detector with 120 mm diameter.

2.3 Photodissociation of SO_2 at 193 nm

2.3.1 Introduction

We first tested our new apparatus with the photodissociation of sulfur dioxide (SO_2) at 193 nm to examine the detection efficiency and resolution. The transition of $SO_2(\widetilde{C}^1B_2 \leftarrow \widetilde{X}^1A_1)$ begins around 240 nm with the products of SO ($^3\Sigma^+$) and O (^3P_J) at the threshold around 219 nm (5.66 eV) discussed by Okabe et al[54]. Dynamic measurements between 193 nm and 218 nm with several experimental techniques[61, 33] have been conducted in this range. At these energies, there is insufficient the excess energy to produce electronically excited products.

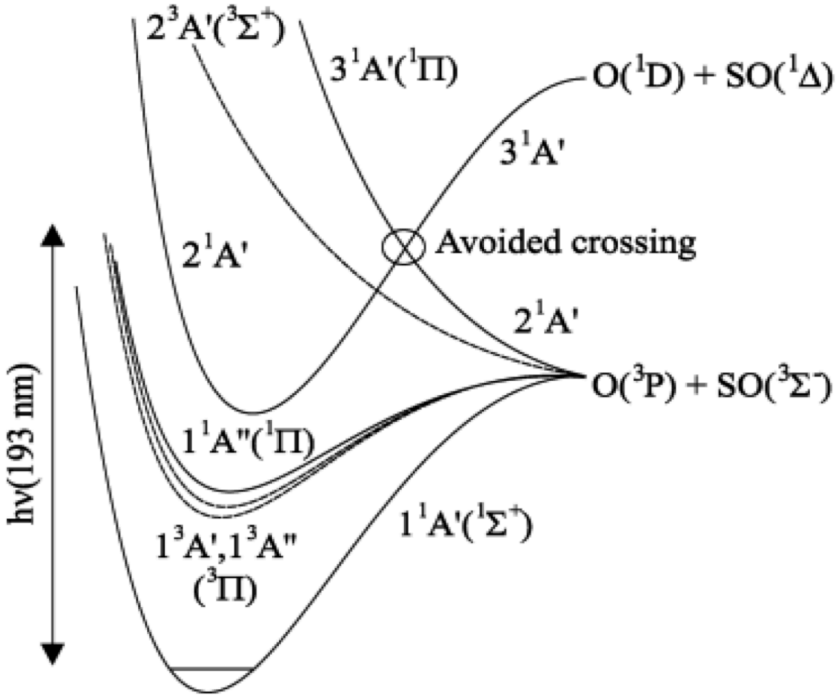

Figure 2.2: Schematic potential surface of SO_2 predissociation adapted from Brouard[9].

The electronic potential surface of SO_2 with some low-lying electronic states is shown in Fig. 2.2. There are several arguments focusing on the SO_2 predissociation

mechanism which is not well understood: there may be internal conversion to the ground electronic state $\widetilde{X}^1A_1$, intersystem crossing through a triplet state ($2^3A'$) and inferral crossing to a singlet state (3^1A_1).

Katagiri et al.[35] summarized some previous work and investigated the photo of SO_2 using the laser induced fluorescence (LIF) spectrum of $\widetilde{C} - \widetilde{X}$ band with some theoretical calculations. They concluded the dominant mechanism was the internal conversion between the $\widetilde{C}$ band and the ground state $\widetilde{X}$, but there may be additional dissociation channels through the crossing the triplet state ($2^3A'$) and that through a singlet state (3^1A_1). More experiments conducted with quantum beats and measurements of fluorescence lifetime and quantum yield[64, 73] imply the major channel of the predissociation was through the internal conversion to the ground state.

The photodissociation of SO_2 was also investigated by the VMI technique. In 2000, Houston et al.[19] studied the reaction by REMPI of O (^3P_J) atoms at the photolysis wavelength between 202 and 207 nm. The conclusion of their research was a disagreement with most previous work. They suggested two different predissociation mechanisms related to the change of internal energy and the dominant mechanism below 203 nm was an avoided crossing with the singlet state (3^1A_1). Brouard et al.[9] investigated the photodissociation at 193 nm by REMPI of ground state O (^3P_J) coupled with VMI. They focused on the orbital polarization of O and indicated that the orbital polarization could be from internal conversion or the coupling with triplet state. Some experiments conducted by infrared diode laser to detect the rovibrational transition of SO fragments[33] from the photodissociation of SO_2 at 193 nm agreed with the statement about coupling with triplet state. By time-resolved Fourier transformed infrared emission spectra, the vibrational excited SO fragments were observed from the photolysis of SO_2 at 193 nm by Dai et al.[48] in 2012. They concluded two distinct dissociation machanisms with the product of excited vibrational SO frag-

ments: the internal conversion between between the $\widetilde{C}$ band and the ground state $\widetilde{X}$ and the intersystem crossing to the triplet state.

Another mechanism of the predissociation, the intersystem crossing to singlet state, is suggested by Ray et al.[61] through the dispersed emission spectra. They observed the spectra at the excitation energy around 200 nm lower than the other researchers. The result is different from the other researchers and may be an indication that the repulsive singlet state undergoes an avoid crossing with the $\widetilde{C}$ band.

In summary, the machanisms of predissociation of SO_2 seems inconsistent. It is possible that exists different mechanisms in various wavelength as concluded by Houston et al. In our work, we used SFDC raster imaging to detect SO fragments and obtain the translational energy and angular distribution. The image and the translation energy obtained are used as a calibration for the other experiments.

2.3.2 Experiment

The experimental setup of SFDC raster imaging is almost same as discussed in last section and some details are specified here. The SO_2 (Air Products, liquefied, anhydrous grade) gas sample was seeded with helium at ∼20% concentration by ∼2 bar backing pressure. Helium was utilized as carrier gas to avoid ionization by the probe laser due to its relative high ionization penitential. As discussed earlier, an unpolarized ArF excimer was operated as a photolysis laser at 193 nm with the power ∼3mJ. The probe laser (Ti:sapphire, ∼800nm, 1 kHz,KMlabs, Wyvern 1000) set on the translational stage can be moved ∼11 mm to scan the central slice of the expanded ion cloud with 0.005 mm and 1 ms for each step. The power of the probe laser was reduced by a ND filter to keep the power ∼0.6 mJ in order to avoid the space charge effect when too many products or parents molecules are ionized. The

SO fragments produced during the dissociation event at the ground state were ionized directly to the continuum by the probe laser via strong field ionization between the repeller and the extractor. The voltage of the repeller was maintained at +200 V and for the extractor was +180 V. After SO fragments were ionized, they were accelerated by the repeller through the ion optics and flight tube, then detected by dual MCP coupled with phosphor screen. The image of the products was recorded by a CCD camera operated at 30 Hz. The piezo valve, photolysis laser and the MCP were all synchronized by a delay generator in 100 Hz operation rate.

2.3.3 Results and discussion

Fig 2.3 shows image of the SO ($^3\Sigma^+$) photofragments from the photodissociation of SO_2 at 193 nm. The center spot in the image is the SO fragments from the SFI of SO_2 because when the probe light scanned over the molecule beam, it generated some fragmentation with SO generated. The ring in the figure indicates an almost isotopic angular distribution with the photolysis laser unpolarized. This is in agreement with the measurement from Kawasaki et al. about the angular distribution of SO photofragment by photodissociation of SO_2 at 193 nm. According to their observation, the anisotropy of the photodissociation event is zero owing to much greater dissociation lifetime compared with molecular rotation time.

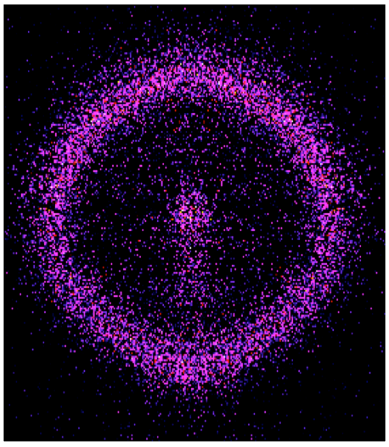

Figure 2.3: Image of SO photofragments from the photodissociation of SO_2.

The anisotropy parameter (β) for the SO ($^3\Sigma^+$) photofragment is extracted from the image with the following equation(Eq(2.1)):

$$I(\theta) = \frac{1}{4\pi}(1 + \beta(P_2(cos\theta)) \tag{2.1}$$

where θ is the angle between the SO fragment velocity and the photolysis light polarization (linear polarized) direction, and $P_2(cos\theta) = (3cos^2\theta - 1)/2$ is the second-order Legendre polynomial. From the analysis, the anisotropy parameter β is around 0.12. Because the photolysis light is unpolarized, the light is mixed with horizontally and vertically polarized lights. The real anisotropy parameter of the photodissociation event should be around 0.24, twice of the result obtained from the image. Brouard et al. measured β and obtained a result around 0.12, which is in fair agreement with our measured value of 0.24.

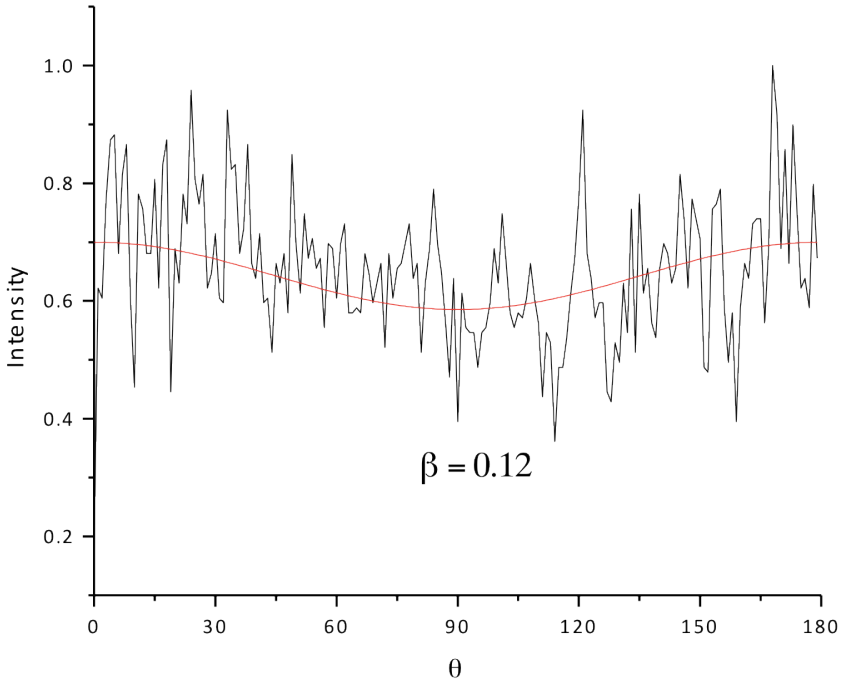

Figure 2.4: The anisotropy parameter of the photodissociation of SO_2 at 193 nm simulated from SO image.

The cofragment in the photodissociation event is O (^3P_J), thus the speed distribution of O (^3P_J) can be obtained from the speed distribution of SO fragment by momentum conservation. In Fig. 2.5, the speed distribution of O (^3P_j) recoiling from SO fragments is compared with the data obtained by Brouard et al. They investigated the 193 nm photodissociation of SO_2 with VMI by REMPI of there spin-orbit states of the ground state O ($^3P_{J=0,1,2}$). The speed distribution from our experiment is comparable with the data obtained by REMPI. The slow component in the speed distribution is from the SO fragment generated by strong field dissociation of SO_2. Then the SO fragment speed distribution is used as a calibration of velocity per pixel to examine the photofragments speed or translation distribution from the other

molecules photodissociation event at 193 nm.

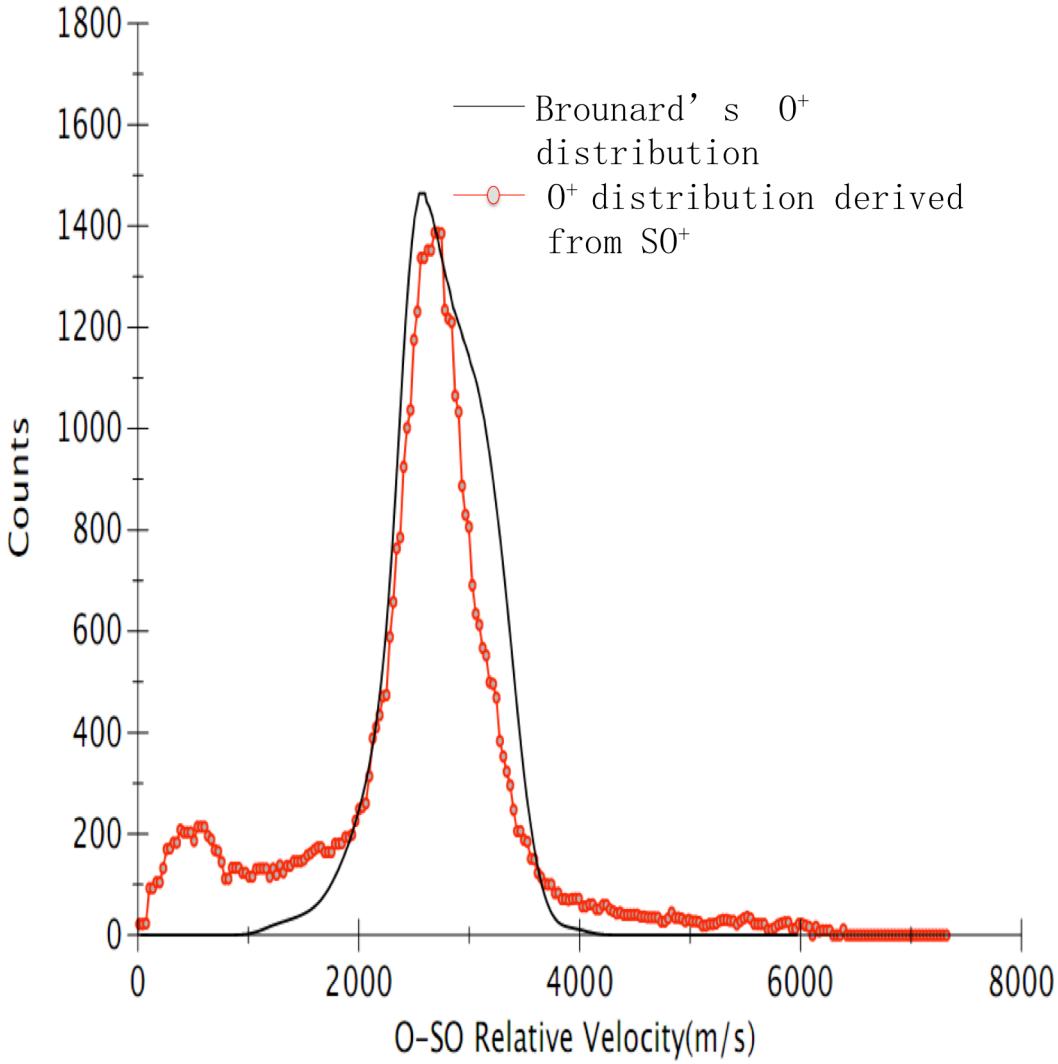

Figure 2.5: Velocity distribution of O(^3P) regenerated from the velocity distribution of SO fragment[9].

2.4 Photodissociation of nitromethane in 193nm

2.4.1 Introduction

Nitromethane has two main transitions in the UV absorption spectrum[31, 57]. One is a weak transition ($\pi^* \leftarrow n$) at ~270 nm[4], and the other one is a strong transition band ($\pi^* \leftarrow \pi$) on the side of NO_2 around 198 nm[51], which is supported by calculation from Flicker[22]. Experimentally, numerous studies focused on the photodissociation process of nitromethane within the $\pi^* \leftarrow \pi$ transition mostly. The primary channel is suggested as the bond cleavage of C-N bond involving the product of methyl radical and excited $NO_2(^2B_2)$. Some researchers concluded other minor dissociation channels producing oxygen or HNO[67]. Blais et al. determined the cross section of C-N dissociation as $1.7 \times 10^{-17}\ cm^{-1}$ at 193 nm via $\pi^* \leftarrow \pi$ transition[7]. Butler et al. measured the translational energy distribution of the product[10] generated from nitromethane photodissociation at 193 nm via product emission spectroscopy and photofragment translational energy spectroscopy. They concluded the excited $NO_2(^2B_2)$ product from the major channel can decay to NO and O spontaneously, given little internal energy in methyl radical generated with $NO_2(^2B_2)$.

Lao et al. observed the resolved emission spectrum from nitromethane via excitation of $\pi^* \leftarrow \pi$ transition at 200 and 218 nm[41]. Their conclusion supported the mechanism proposed by Butler et al. The conclusion from Houston et al. by using REMPI and TOF spectroscopy was also consistent with the earlier result of two channels in the dissociation. They measured the internal energy of methyl and ground state NO ($X^2\Pi$) and translational energy distributions of methyl, excited NO ($A^2\Sigma^+$) and O(^3P) via 193 nm photodissociation of nitromethane. They believed the minor channel producing NO_2 in another excited state generated the products of

excited NO(A) and O(^3P).

There is some theoretical and experimental research related to the infrared multiphoton dissociation (IRMPD) of nitromethane as well. In 1986, Wodtke et al. investigated the dissociation of nitromethane via IRMPD[75]. They suggested another minor channel via the isomerization of nitromethane producing CH_3O and NO. They determined the branching fraction of NO vs NO_2 production was 0.4 and the barrier of isomerization was around 55.5 ± 1.5 kcal/mol, lower than the C-N bond breaking energy (59 kcal/mol). By theoretical calculation, the key question is whether there is a loose or tight transition state during the isomerization. Some research determined this was a tight transition state for nitromethane isomerization to CH_3ONO[20, 49, 53, 32], but some concluded an opposite determination[63]. Recently, M. C. Lin et al.[79] found that in addition to isomerizing to trans-CH_3ONO, CH_3NO_2 can also isomerizes to cis-CH_3ONO by a loose transition state. This loose transition state indicates a roaming mechanism for the isomarization process exists potentially with NO and CH_3O produced.

In our experiment, we detected the NO, methyl radical and oxygen fragments produced from the photodissociation of nitromethane at 193 nm via SFDC slice raster imaging. The translational distribution of each fragment detected will be discussed to determine the mechanism of the photodissociation.

2.4.2 Experimental

The experiment was preformed in the same SFDC slice raster imaging apparatus described in last section. Briefly, a gas sample containing 2% nitromethane seeded with helium was introduced by a piezo valve coupled with a skimmer. After passing through the differential stage via a slit, the molecular beam entered the main chamber

and interacted with the photolysis and probe lasers. The photolysis laser source was a ArF Excimer laser (EX/10) with a power of 0.6 mJ. The probe laser was provided by a femtosecond laser (Ti:sapphire, ∼70 fs, KMLab, Red dragon) with 1.0 mJ power scanning over the central section of the ion cloud. The produces were ionized directly to the continuum. The ions were detected by a MCP/Phor detector and averaged by CCD camera.

2.4.3 Result and discussion

Due to relatively lower ionization potential of nitromethane compared with the photofragments (i.e. methyl radical, NO and O et al.), when the probe laser scanned over the central slice of the ion cloud vertically, it was moved about 1.5 mm with the faster speed when it met the molecular beam to avoid too much fragmentation from the strong field dissociation of parent molecules, which produced a gap in the center of the images.

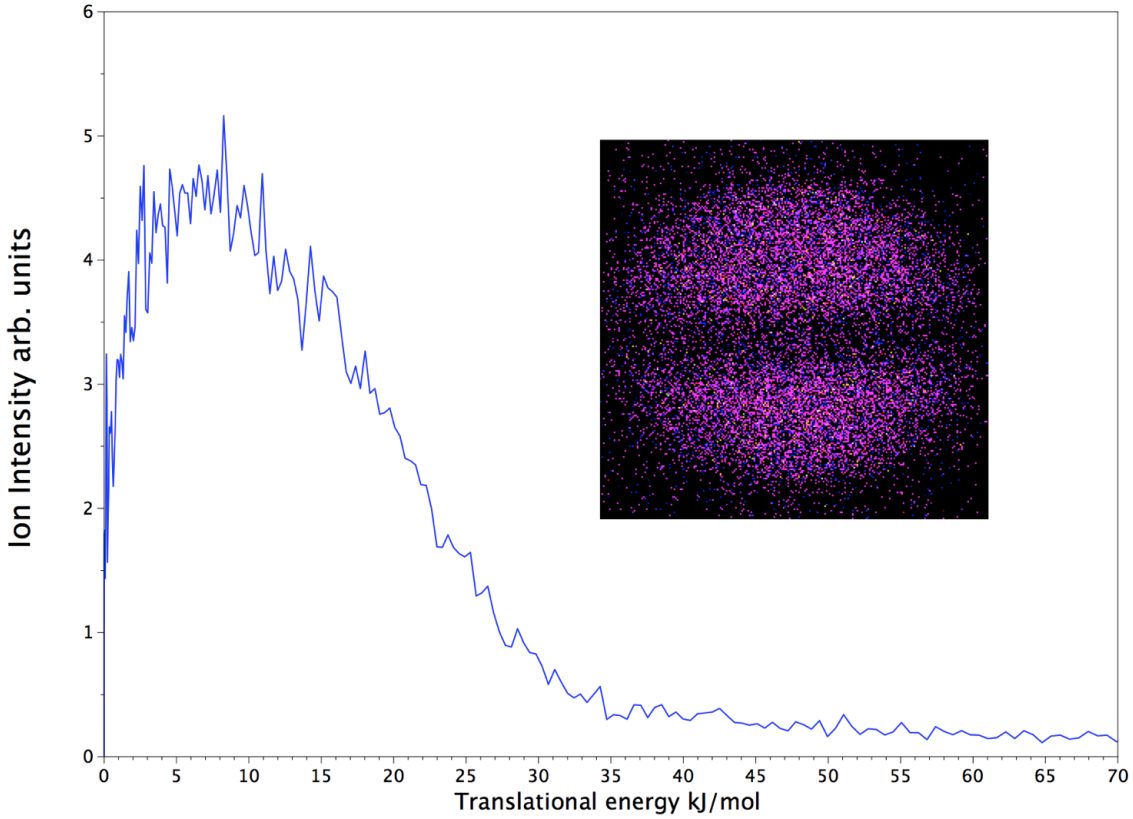

Figure 2.6: Image and translational energy distribution of methyl radical by SFDC raster imaging.

Fig 2.6 shows the image of methyl radical and its translational energy distribution derived from the image of methyl radical. It has a broad distribution from zero to ∼30 kJ/mol with a peak around 8 kJ/mol.

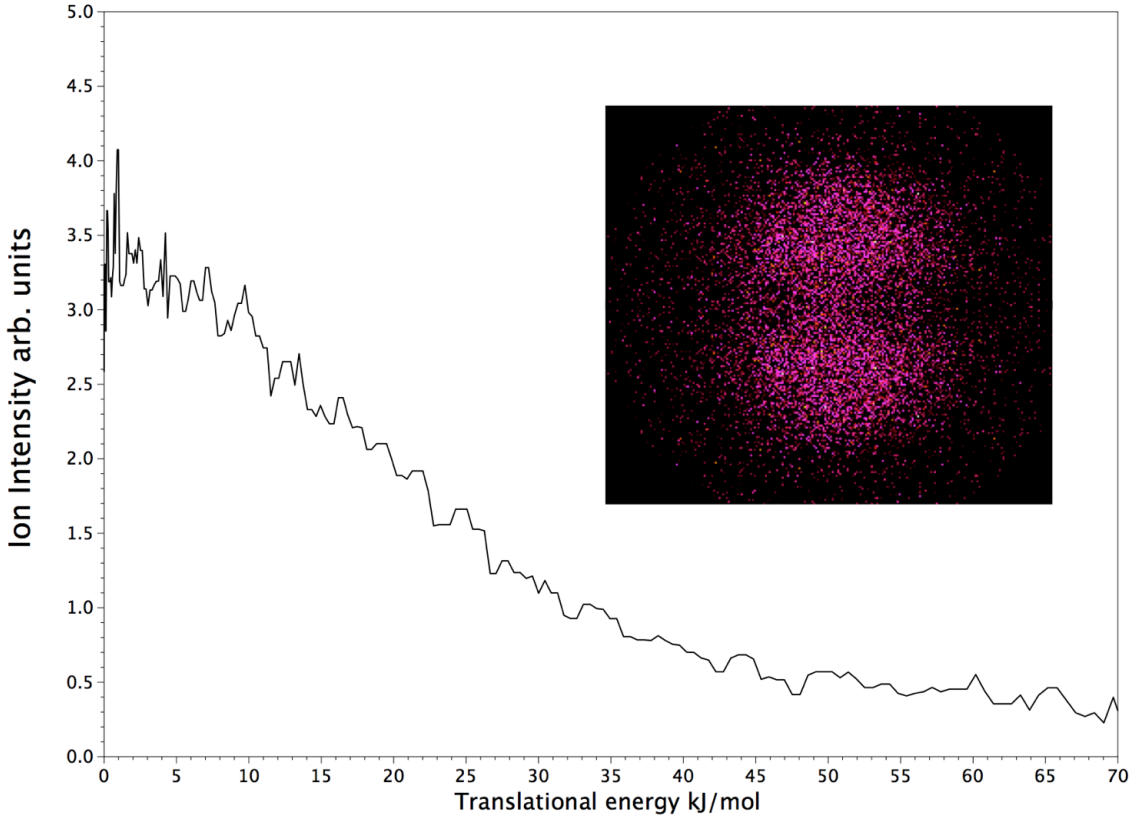

Figure 2.7: Image and translational energy distribution of NO by SFDC raster imaging.

The image and translational energy distribution of NO are shown in Fig. 2.7. There is a feature around 3 kJ/mol with a broad distribution to 40 kJ/mol. The averaged value of this translational energy distribution is ∼23 kJ/mol. Because in SFI, it is hard to operate state selective detection of the fragments due to the direct ionization to the continuum state. The NO fragments detected by SFI that included all the NO products in different electronic states. We also detected some signal at mass-to-charge ratio (m/z) = 16 indicating the detection of O atoms. Figure 2.8 displays the translational energy distribution of oxygen atoms from the photodissociation with a peak at 8 kJ/mol and a broad distribution to 25 kJ/mol.

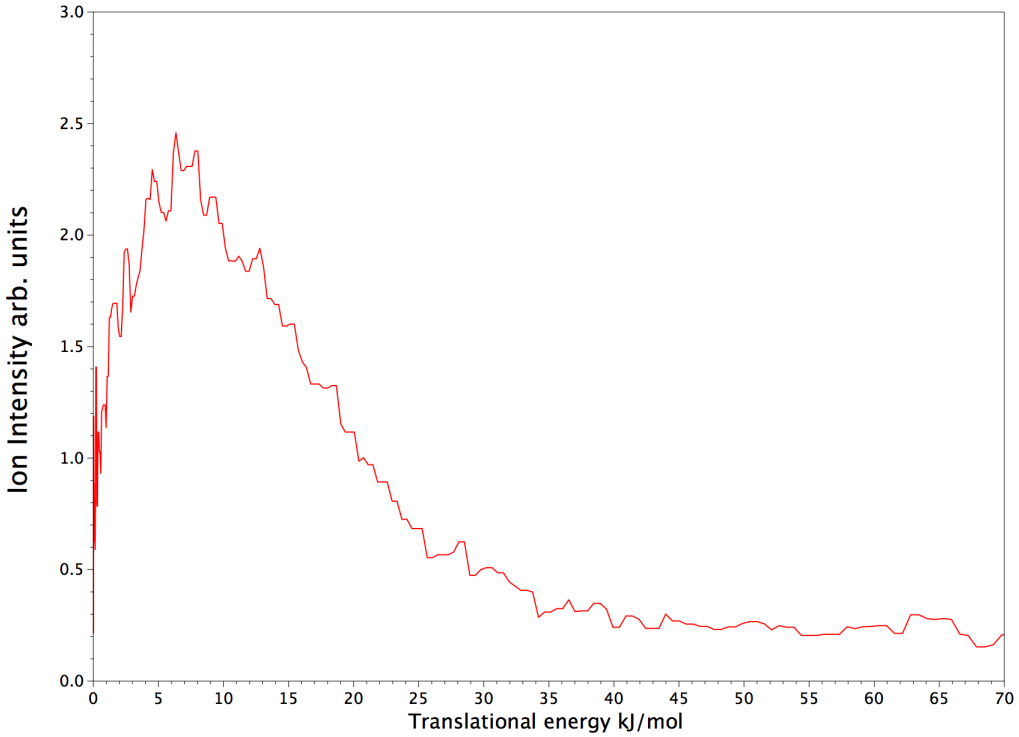

Figure 2.8: Translational energy distribution of O by SFDC raster imaging.

The broad translational energy distribution of methyl may indicate not only one mechanism in the photodissociation event. In 193 nm $\pi^* \leftarrow \pi$ transition, the C-N bond cleavages with the products of ground state methyl and NO_2 is suggested as the primary channel. Some NO_2 produced in this channel with more internal energy can experience unimolecular decomposition with NO and O.

The available energy of one 193 nm photodissociation process can be expressed as

$$E_{avail} = h\nu + E_{int}^{P} - D_0(R - NO_2) = E_E + E_T + E_V + E_R \tag{2.2}$$

with the conservation of energy, where E_{avail} equals the photon energy of 193 nm plus E_{int}^{P} (the internal energy of parent molecules) minus the energy needed to break C-N bond. During the photodissociation process, the available energy is partitioned

into the translational, electronic, vibrational and rotational degrees of freedom of the photofragments. In the supersonic molecular beam, the internal energy of parents can be estimated to be zero, and for the photofragments, the internal energy of methyl is assumed to be zero with ground state CH_3 from the observation of Houston et al. With 250 kJ/mol of the C-N bond break energy obtained by M.C. Lin et al. (Fig. 2.9), if we use the lower translational energy of methyl around 8 kJ/mol with $D_{0(NO-O)} = 301 kJ/mol$, the translation energy of NO_2 should be around 49 kJ/mol. Because of the momentum conservation, the energy partitioned into NO and O including translational and internal energy should be 17 kJ/mol and 32 kJ/mol, respectively. From the experimental translational energy of NO in Fig 1, there is some NO products with lower translational energy lower than 17 kJ/mol, corresponding to the ground electronic state of NO(X). This is the product from unimolecular decomposition of NO_2 from the major channel. This conclusion is consistent with the observation of Butler et al.[10] and Houston et al.[50]

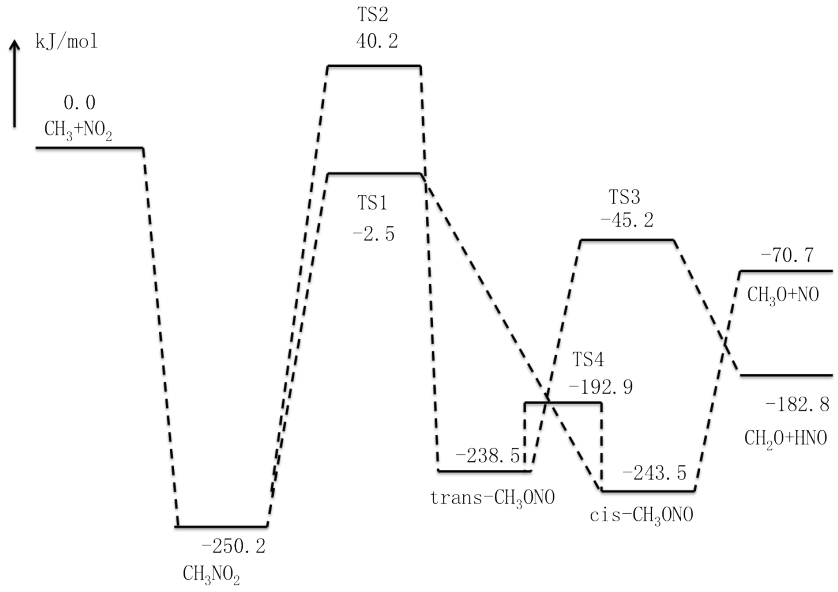

Figure 2.9: Schematic energy level of nitromethane dissociation computed at the UCCSD(T)/CBS level. (Adapted from [79])

Another minor channel suggested by Butler[10] is the multiphoton dissociation of NO_2 product with NO and O generated. In this process, the NO_2 can absorb another 193 nm photon and be excited to another state, and then it dissociates to NO(A) and O(^3P), corresponding to the faster component observed in NO translational energy distribution. In our data for the NO translational energy distribution, the averaged tranlational energy is ∼23 kJ/mol with intense signal beyond 17 kJ/mol which cannot be explained by the spontaneously decay of NO_2 in the primary channel. One way to explain that is the NO product from the multiphoton dissociation of NO_2 gained more available energy partitioned into the tranlational energy of the products. In this process, the NO products could be produced at the NO(A) excited state.

In addition, there may be other channels based on the theory by M.C. Lin et al.[79]. Their result indicates nitromethane can isomerize to cis-CH_3ONO by a very loose transition state lying ∼2.5 kJ/mol below the C-N bond rupture channel. Their loose transition state is similar to a "roaming" mechanism[28] during the isomerization. The available energy in this process in single photoionization at 193 nm is 439 kJ/mol, which can be partitioned into the internal and translation products of methoxy radical and ground state NO. The NO generated in this process should be with more translational energy. This isomerization-mediated roaming mechanism has been discovered in the photodissociation of nitrobenzene at 226 nm[28]. However, it could be a potential channel which can compete with the breaking C-N bond channel in the photodissociation process of nitromethane at 193 nm.

2.4.4 Conclusion

We reported a new ion imaging technique named SFDC slice raster imaging to investigate the photodissociation of nitromethane at 193 nm. The translational en-

ergy of methyl radical, NO and O were measured with the images obtained and they were consistent with the previous experiment results. We conclude that the NO fragments can be produced via at least two channels: NO_2 spontaneous dissociation with sufficient energy in the single photon process is the primary channel, and there is multiphoton dissociation of NO_2 with another 193 nm photon energy in the dissociation process. It is possible that other mechanism of NO production may exist. More investigations are needed to explore this multichannel photodissociation process.

Chapter 3

ATOMIC ORIENTATION DEPENDENCE OF STRONG FIELD IONIZATION

3.1 Introduction to strong field ionization rate dependence

3.1.1 Atomic alignment and orientation

The process of strong field ionization (SFI) can be interpreted by a two-step model. First, a intense laser field suppresses the Coulomb potential of the atom, which results in the tunneling of a bound electron to the continuum. Second, the free electron with zero initial kinetic energy is accelerated by the laser field and receives a linear momentum that is only related to laser field strength at the tunneling time. There are several models developed to simulate the ionization process for atoms in the intense laser field: the Amosov-Delone-Krainov (ADK)[1] model, the barrier suppression ionization (BSI)[2] model and the Keldysh-Faisal-Relss (KFR)[5] model. These may be used to predict the ionization rate in SFI. All of them conclude that the ionization rate for atoms depends on the alignment of electronic orbitals, which is described by the distribution of the absolute value of the magnetic quantum number,

$|m|$, in a linearly polarized field[5] (Eq (3.1)):

$$\omega \propto (\frac{(2l+1)(l+|m|)!}{2^{|m|}|m|!(l-|m|)!})(\frac{3F_0}{\pi F})^{\frac{1}{2}}(\frac{2F_0}{F})^{2n-|m|-1}e^{\frac{2F_0}{3F}} \tag{3.1}$$

where ω is the ionization rate, $F_0 = (2E_0)^{\frac{3}{2}}$, E_0 is the ionization potential, F is the laser field strength, n is the principle quantum number, l is the angular momentum quantum number and m is the magnetic quantum number. L. Young et al.[78] observed orbital alignment dependence of krypton atoms generated in strong-field ionization by the absorption of X-ray and E. Gouliemakis et al.[23] reported the density matrix in atomic krypton ions of valence electron motion by the measurement of attosecond extreme-ultraviolet pulse absorption. The sensitivity of orbital alignment is also observed from xenon atoms by SFI using high-order harmonic transient absorption spectroscopy[46]. Recently, we demonstrated this sensitivity by measuring the angular dependent ionization rate of sulfur atoms produced from photodissociation of carbonyl sulfide and ethylene sulfide[44].

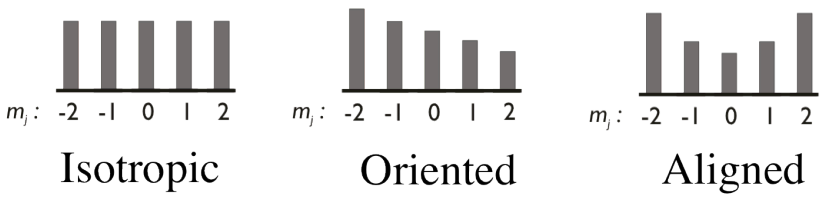

Figure 3.1: Schematic diagram of isotopic, alignment and oriented atoms.

However, the sensitivity of strong field ionization to atomic orbital orientation or helicity, which is proportional to the net magnetic moment determined by the sign of magnetic quantum number, is less obvious. There has been no previous experimental work and only some theoretical treatments. Although there was an explicit formula for strong field ionization developed by Tulenko et al.[71], the formula still does not

include the sign of m, only the dependence on the absolute value of m. There was a theoretical paper published recently by Bath et al.[3] who first developed a formula for SFI containing an anisotropic m distribution and discussed the dependence of ionization rate of the atomic orientation. They predicted the strong-field ionization rate of $m = -1$ orbital in a right polarized light field is three times higher than that of $m = 1$. In fact, it has already been reported that in weak field limit the circularly polarized light given a higher ionization rate for the corotating electron (i.e for positive m, higher ionization rate with right circularly polarized light) in single-photon ionization and field ionization of Rydberg states.

Understanding the dependence of strong field ionization on atomic orientation is important to many aspects of chemical dynamics. Aligned or oriented atomic fragments are produced in the process of photodissociation and the products reflect the details of the dynamics such as state symmetry, curve crossing and coherence. The traditional method to probe the aligned/oriented atoms is using REMPI without any time-resolution. By SFI detection, it is possible to provide more details about the chemical dynamic process in the real time electron density rearrangement with time resolution of the m distribution. The sensitivity of orbital orientation in SFI is also very important to the field of attosecond dynamics because circularly polarized light may play a role in generation of isolated attosecond pulses.

3.1.2 Sequential and non-sequential double ionization

As discussed earlier, in an intense laser field, a electron can tunnel out through the Coulomb barrier when the potential surface is suppressed by the laser field. If there is another electron ejected from the parent atom after the single cation formed, it is a sequential double ionization (SDI) process because there is no interaction between

the two electrons and the two electrons are removed from the parent independently and sequentially.

Another process is non-sequential double ionization (NSDI) with both electrons ejected simultaneously, especially in the linearly polarized laser field. After the first electron is removed from the parent atom, it will be accelerated in the laser field and gain considerable kinetic energy with the momentum. When the electric field changes the sign, the free electron will be driven back to the parent ion. After the recollision with the parent ion, the electron can collide with another electron and both of them will rescatter to form the double cation. This is a polarization dependent mechanism because in the circularly polarized laser field, the rotating electron field prevents the free electron from being driven back to the parent ion so the non-sequential double ionization process is strongly suppressed. This has already been observed in the experiments.

We can exploit sequential double ionization using the strong field both to prepare an oriented ion and to probe it (Fig. 3.2). The sequential double ionization yields of argon are compared using two nearly circularly polarized laser pulses with the same or opposite helicities. If there is a higher ionization rate with a certain sign of the magnetic quantum number, the single cation generated by the first pump pulse will have oriented orbital angular momentum (with anisotropic m distribution). The probe laser pulse will detect this anisotropic distribution and the difference of total ion yield of argon double cation will be observed depending on the same or opposite helicities of pump and probe laser pulse.

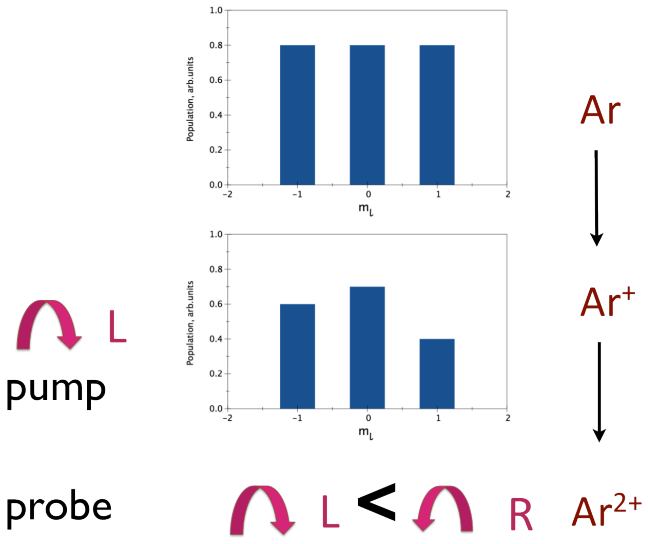

Figure 3.2: Schematic diagram of argon sequential double ionization by two nearly polarized laser field.

3.2 Experimental Setup

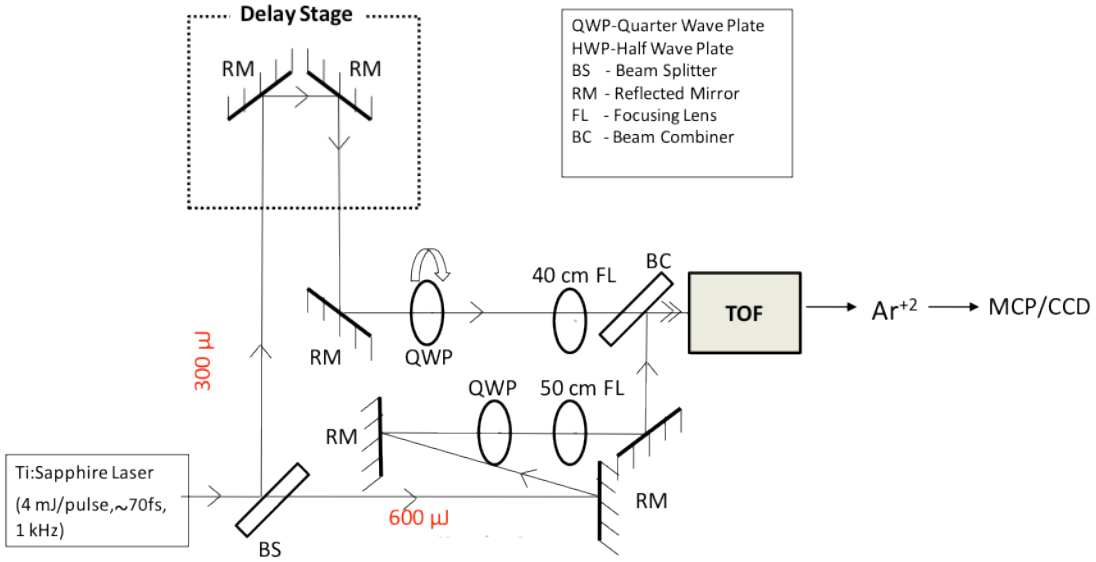

Figure 3.3: Diagram of the designed pump-probe setup using circularly polarized laser field.

The experiment is carried out using a modified velocity map imaging apparatus, but we only use it here as a TOF spectrometer to measure the ion yield. The source chamber and main chamber are pumped by two turbo-molecular pumps, respectively. The continuous argon beam is introduced by expanding argon through a 20 micron diameter nozzle coupled with a skimmer and then the argon are ionized by laser beams between the repeller and extractor electrodes of the TOF mass spectrometer. The infrared laser beam is a 4 $mJ/pulse$, $\sim 70fs$, 1 kHz with a Ti:sapphire amplification system, and it is split into two beams as pump and probe, with the power of 300 μJ and 600 μJ, respectively (Fig. 3.3), using a Mach-Zenhnder type interferometer. The focused laser intensities of pump and probe laser beam are $\sim 9 \times 10^{13} W/cm^2$ and $1.4 \times 10^{14} W/cm^2$, with 40 cm and 50 cm focal lens, respectively. To achieve SDI, the laser intensity of pump beam is lower than that of the probe beam to avoid NSDI. The pump beam ionizes the argon atom to single charged cation at first, then the probe beam ionizes the single cation to double cation. Both of them are nearly circularly polarized via two separate quarter wave plates. The measured ellipticity of the probe beam is $\sim$0.8. The helicity of the pump beam is changed by rotating the quarter wave plate in front of the focal lens by 90 degrees. The measured ellipticities of the pump beam with right and left circularly polarization are 0.88 and -0.80, respectively.The pump and probe beam are collinearly circularly polarized and delayed by a motored translation stage with continuous translation and recombined in front of the TOF spectrometer. After the argon ions generated by both laser beams fly through the 20-cm-long field free time-of-flight tube, they are detected by an MCP coupled with a phosphor screen, and a charged coupled device (CCD) camera averages the signal

coupled with IMACQ[42] acquisition program.

3.3 Results

In Figure 3.4, we show the time dependent trace of argon dication yield. The negative number of the pump-probe time delay indicates the probe beam is earlier than the pump beam initially. The time delay of the probe beam is changed by a translation stage with the pump beam fixed. When the probe beam is moved to overlap the pump beam temporally, extensive signal of argon dication is produced due to the non-sequential double ionization. When the probe beam is later than the pump beam, the argon dication yields of the same and opposite helicity of both beams are compared. For analysis, we use a time delay more than 500 fs to avoid any nonsequential double ionization.

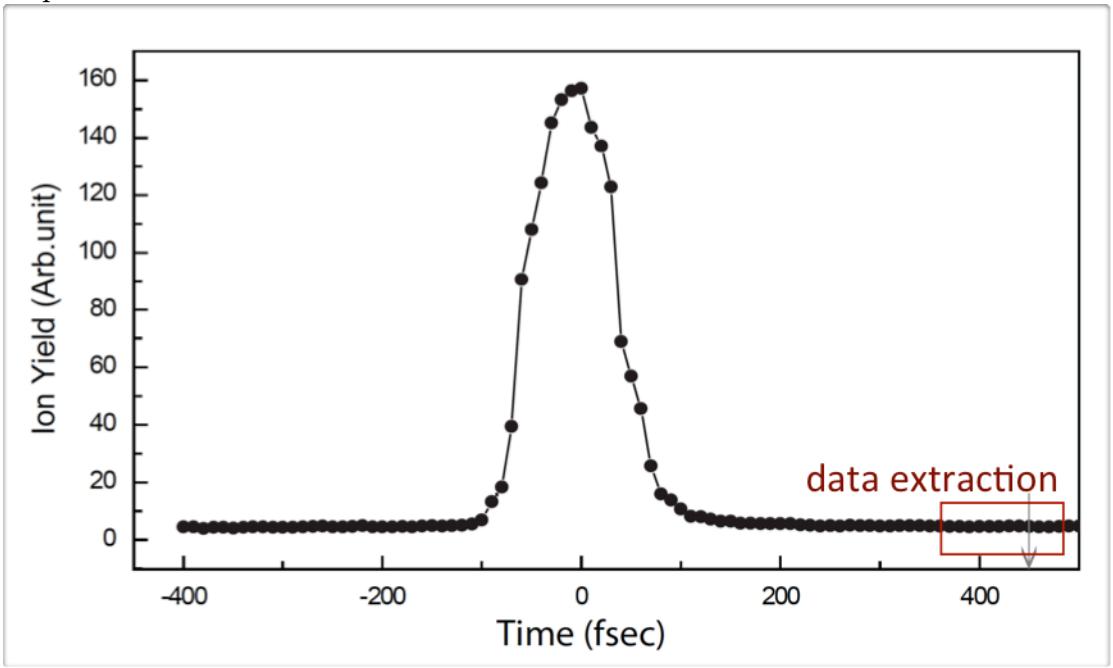

Figure 3.4: The time dependent Ar^{2+} yield. The grey arrow marks the time delay used for the data extraction.

We measured the ion yield of argon dication under four laser conditions: both lasers on (I_{pp}), pump beam off (I_{pu}), probe beam off (I_{pr}) and both beam off (I_d, dark counts). The ion yield of argon dication was averaged for ten data sets under each conditions for 200 seconds each, shown in Fig 3.5. The yield of argon dication was calculated by using the equation $I_{SDI} = I_{pp} - I_{pr} - I_{pu} + I_d$.

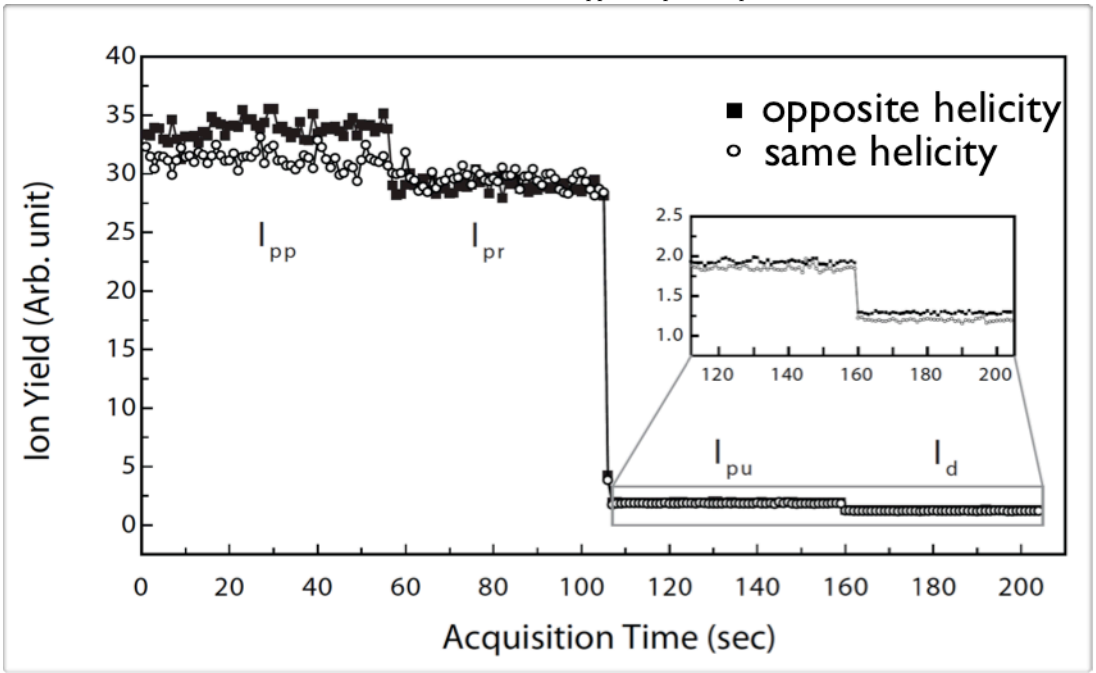

Figure 3.5: The ion yield of Ar^{2+} under different laser conditions. The inset is a zoom-in of the ion yields with the probe laser blocked and both laser blocked.

I_{SDI-LR} is used to represent the ion yield of argon dication obtained for opposite helicity between the pump and probe laser beams and calculated as 4.21±0.98 in arbitary units. For I_{SDI-RR} , it is 1.16±0.92. The experimental I_{SDI-LR} and I_{SDI-RR} are clearly distinct. The single argon ion yield generated by pump beam alone in right and left circular polarization is measured to rule out the slight ellipticity difference. The difference is only <3% between the right and left circularly polarized light, and it is consistent with the argon dication yield generated by only the pump beams (I_{pu}), ∼4% difference between two helicities. Hence, the difference (>300%) observed in

the SDI of argon is indeed produced by the difference in relative helicity between the pump and probe beams. Another way to explain the result is the pump beam first ionized the argon atom by removing a electron with one sign of m, then the probe beam with opposite helicity can further ionize the sublevel with the opposite sign of m. However, for the probe beam with the same helicity, the ionization rate is lower because a given m sublevel has been already reduced by the pump beam.

3.4 Discussion

To further analyze the data, we need to establish a relationship between the ionization rate and the argon double cation yield obtained from the experiment. We also need to extract the ionization rate ratios between the sublevel of $m = -1$ and $m = 1$ in the circularly polarized laser field. The electrons are ionized from the argon $3p$ subshell, with magnetic quantum numbers: $-1, 0, +1$. The ionization rate from these sublevels in right circularly polarized light can be labeled as ω_{-1R}, ω_{0R} and ω_{+1R}, respectively. By symmetry, the assumption $\omega_{-1R} = \omega_{+1L}$, $\omega_{0R} = \omega_{0L}$, $\omega_{+1R} = \omega_{-1L}$ should be true. Then, the ratio of argon double cation yield between two different helicity configurations can be written as:

$$\frac{I_{(SDI-LR)}}{I_{(SDI-RR)}} = \left(\frac{(\alpha+\beta)\alpha' + (1+\alpha)\beta + (1+\beta)}{(1+\beta)\alpha' + (1+\alpha)\beta + (\alpha+\beta)}\right) \tag{3.2}$$

where, $\alpha = \omega_{(-1R)}/\omega_{(+1R)}, \alpha' = \omega'_{(-1R)}/\omega'_{(+1R)}, \beta = \omega_{0R}/\omega_{(+1R)}, \beta' = \omega'_{0R}/\omega'_{(+1R)}$. The prime denotes the ionization rate related to the probe laser beam, because the ionization rate of pump and probe beam should be different due to different ionization potential and laser intensities. Compared with the ionization rate of $m = -1$ and $m = +1$, the ionization rate of m=0 is very small based on the calculation by Barth

et al. Thus, β and β' approach zero, and we obtain the simpler equation (Eq (3.3)):

$$\frac{I_{(SDI-LR)}}{I_{(SDI-RR)}} = \frac{(\alpha\alpha^{'} + 1)}{(\alpha + \alpha')} \tag{3.3}$$

If the ratio is 1, that indicates there is no dependence of the ionization rate on the signs of the magnetic quantum number. Therefore, there should be no enhancement in the observed ion yield. If the ratio is non-unity, this implies strong field ionization for circularly polarized light involves a higher ionization rate for one sign of m over the other, for both neutral atoms and for single ions. From the experimental data, the ratio obtained is 3.63. If we substitute this value into the simplified equation (Eq (3.3)), the values of α and α' can be obtained and the plot of α vs α' is displayed in Figure 3.6. If we assume $\alpha \simeq \alpha'$, we get the point shown on the hyperbola. The theoretical value is also shown on the plot and discussed below. Both ratios are higher than 3.63 while the exact values depend on their positions at the hyperbola. The ratios more than unity indicate that in the processes of ionizing neutrals and single ions by circularly polarized light, the same sign of m is preferred.

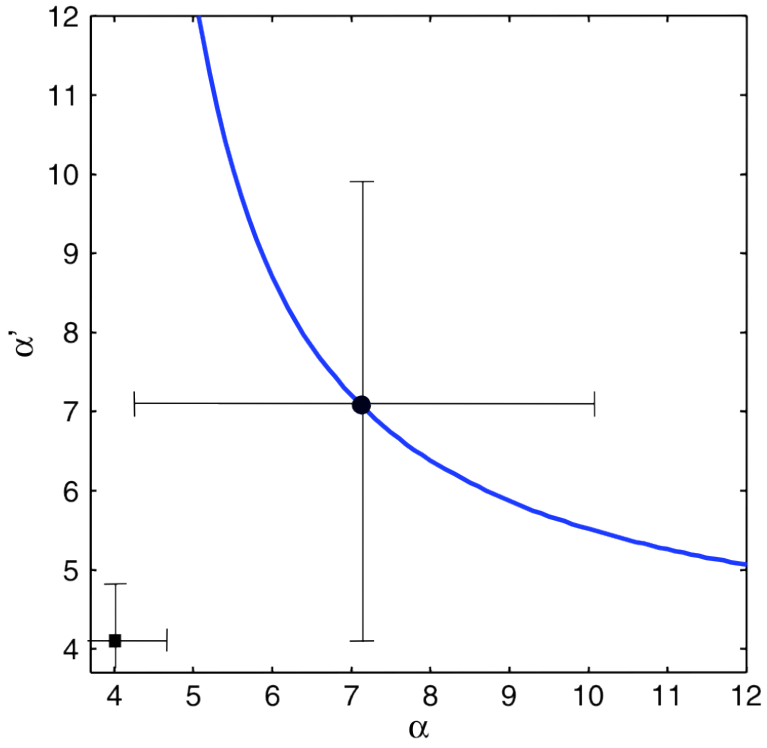

Figure 3.6: The experimentally constrained ratios of strong-field ionization rates between m=1 and m=-1 sublevels of neutral argon atom and argon single ion by right circularly polarized light.

Another needs to be emphasized here is that it is not possible to identify which sign of m given a higher ionization rate. Due to the symmetry of the equation with simplification, the equation would not be changed if we inverse the definition of α and α'. To identify the exact preference of which sign of m, we need to measure the ionization rate of some orientated atoms with a known helicity in some photodissociation process, such as ICl[60] and O_3[39].

We also may compare our measurement with the prediction from theory. The Keldysh parameter γ for our pump and probe laser intensity for argon is $\sim$1.2 and $\sim$1.3, respectively. In the discussion of Barth et al. [3], the ionization rate of a p level can be calculated by the equation below:

$$\omega_{p_m}(E,\omega) = I_p|C_{\kappa l}|^2 \frac{E}{2E_0} h_{p_m}(\gamma) e^{-\frac{2E_0}{3E}g(\gamma)} \tag{3.4}$$

where $E_0 = (2I_p)^{3/2}$, $\kappa = \sqrt{2I_p}$, $C_{\kappa l}$ is the characterization of the asymptotic behavior of the radial wave function, which is related to orbital quantum number l. The function in the exponent is:

$$g(\gamma) = \frac{3\zeta_0}{\gamma^2(1-\zeta_0^2)} \sqrt{(1+\gamma^2)(\zeta_0^2/\gamma^2+1)} \tag{3.5}$$

The factor including the sign of m is $h_{p_m}(\gamma) = h_s(\gamma)\frac{3(1+\gamma^2)}{2(1-\zeta_0^2)}(\sqrt{\frac{\zeta_0^2/\gamma^2+1}{1+\gamma^2}} \mp \frac{\zeta_0}{\gamma} sgn(m))^2$. ζ_0 is a parameter must satisfy the equation $\sqrt{\frac{\zeta_0^2+\gamma^2}{1+\gamma^2}} = tanh\frac{1}{1-\zeta_0}\sqrt{\frac{\zeta_0^2+\gamma^2}{1+\gamma^2}} (0 \leq \zeta_0 \leq 1)$. Then α and α' can be obtained by the ratio of ionization rate of sublevel $m = +1$ and $m = -1$ of pump and probe beam from the equation by substituting the appropriate Keldysh parameter into the equation. This gives values for of α and α' of 4.0 and 4.2 for the pump and probe laser, respectively. The ion yield ratio is 2.17 by substituting these two ratios into the equation (Eq. (3.3)). If we assume α is nearly equal to α' due to the similar Keldysh parameters (1.2 and 1.3) in our experiment (Fig. 3.6), we obtain $\alpha \approx \alpha' = 7.1$, which is almost twice the theoretical value. The uncertainty in the experiment is large because of the approximations of laser intensity and focal volume averaging. Therefore, we can conclude the result from the experiment agrees reasonably well with the prediction of theory.

However, we should include the laser intensity averaging and focal volume into the comparison of the experiment and the theory to achieve more realistic comparison. Here we try to show how the laser intensity averaging influences the ion yield ratio. The laser pulse used to estimate the ionization ratio is Gaussian-shaped with a 70 fs full width half maximum (FWHM), and a temporal intensity profile of $F(t)$. To

match the average intensity measured in the experiment with the integration of the total pulse envelope, the peak intensity is adjusted. We use the same form of Eq (3.3) and just replaced α and α' with the ionization probability ratios, which are computed as $\chi = \int \omega_{-1R}[F(t)]dt / \int \omega_{+1R}[F(t)]dt$ and $\chi' = \int \omega'_{-1R}[F(t)]dt / \int \omega'_{+1R}[F(t)]dt$. The $\omega_{-1R}[F(t)]$ ($\omega'_{-1R}[F(t)]$) and $\omega_{+1R}[F(t)]$ ($\omega'_{+1R}[F(t)]$) are the ionization rates of $m = -1$ and $m = +1$ for the pump and probe beams at an intensity of $F(t)$, respectively. The ionization yield ratio result from this integration between the two helicity configuration is 1.56. It is smaller than both the result (3.63) from the experiment and the result (2.17) from the calculation of theory. Another point that will further reduce the ratio is the averaging of the focal volume. Although there is a fair agreement between theory and experiment, a rigorous calculation will require better signal-to-noise ratio and beam characteristics

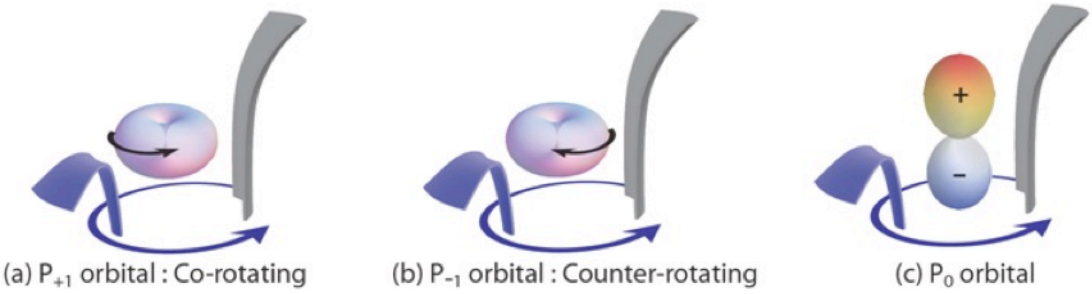

Figure 3.7: The relative rotation between the electrons and the laser polarization can affect the ionization probability if the suppressed Coulomb barrier is viewed as a doorway for tunneling. (a) Corotating electrons and the suppressed Coulomb barrier reduce the ionization rate. (b) Counter-rotation enhanced the ionization rate. (c) The opposite phases of the $p_z(p_0)$ orbital lead to a destructive interference and thus a reduced ionization rate.

There is an intuitive way to understand the preference of m in strong field ionization by circularly polarized light. In this picture, the suppressed Coulomb barrier (SCB) is considered as a "doorway" for the electron to "tunnel" under the barrier to the continuum (Figure 3.7). However, this doorway is not fully open and it is only

with a certain probability (P) that electrons can tunnel out even though they are spatially close to this doorway. This doorway is rotating at the frequency of the laser in circularly polarized light. For rotating electrons with nonzero magnetic quantum number, the helicity is determined by the sign of m. The encounter frequency between the electrons and the suppressed barrier (γ) can be affected by the relative helicity between the electrons and the photons. We use the equation $\gamma = \nu_e^{\pm\nu_L}$ to estimate the encounter frequency, where ν_e, and ν_L are the frequency of the electron rotation and the laser frequency, respectively, and the plus sign means the opposite helicity. The final ionization probability is estimated to be γP. By this simple picture, we can approach several conclusions: (i) electrons counter-rotating with the laser helicity will be preferably ionized; (ii) The ionization rate increases with the laser frequency for counter rotating but decreases for corotating electrons while the ratio between them increases; (iii) the ionization rate for m = 0 sublevel is greatly reduced due to a destructive interference. These results are in general agreement with the previous theory.

In summary, we discovered that the strong field ionization rate of circularly polarized light depends on the relative helicity of the photon and the electron. The conclusion is obtained by measuring the ionization yield of argon dication with two spatially overlapped but temporally delayed near circularly polarized lasers. From the results, we conclude that the ionization rate for both argon neutral and ion is enhanced for the same sign of the magnetic quantum number although this sign is undetermined in the experiment. In the future, the experiments of krypton and xenon will be investigated to explore the effect of the spin-orbital coupling on the ionization rate by circularly polarized laser.

Chapter 4

ISOMER SPECIFIC DETECTION VIA "SEMI-SOFT" IONIZATION

4.1 Introduction to isomer specific detection

4.1.1 Isomer specific detection via synchrotron radiation and electron impact.

Isomer specific detection has already been investigated by synchrotron radiation and electron impact technique for many years. In synchrotron studies, the "soft" vacuum ultraviolet photoionization is used to generate the full shape of the photoionization efficiency (PIE) curves. It is an efficient way to detect the complex mixtures of isomers and related compounds in flame studies and kinetics experiments and operated by Advanced Light Source (ALS)[8, 30, 65].

In 2003, T. Cool et al. first implemented synchrotron radiation to investigate hydrocarbon flame chemistry by flame-sampling photoionization mass spectrometry (PIMS) at the ALS[14, 17, 16, 15, 66, 37, 55, 56, 25, 26, 34, 70, 62]. This approach is widely exploited at the National Synchrotron Radiation Laboratory in Hefei, China as well[58, 59, 77, 43, 68, 13]. By using synchrotron radiation, the photoionization energy is tunable from 8 eV to 15 eV continuously and thus not limited by current VUV laser sources. The advantages of this technique are its extensive signal to noise

ratio and it is a "soft" ionization, which means the species in the flames only undergo single photoionization with minimal fragmentation. With synchrotron radiation single photoionization, the photoionization efficiency (PIE) curve at a mass-to-charge (m/z) ratio of a gas mixture is produced with photon energies varying in a certain range. PIE curves provided by known samples under well-defined conditions were used as "basis functions" to identify the isomeric composition of unknown mixtures or products in flames or kinetics studies.

Another traditional ionization technique, electron impact ionization, is a "hard" ionization technique, which always produces extensive fragments[6, 11]. The signal intensities decline precipitously near threshold, although the use of fixed low energy electron impact has been applied to achieve some selectivity in product detection in limited instances. In general, the selectivity of electron impact for identifying the isomeric of a complex mixture is limited.

4.1.2 Mass spectrometry with a femtosecond laser source

In recent years, using shaped femtosecond laser pulses to achieve isomer specific identification was explored by several groups but not widely used[27, 38, 74]. The potential of using a femtosecond laser is that the experiment would not be limited to synchrotron undulator beamlines and can be operated by routine laboratory applications. In the intense laser field, some molecules undergo extensive fragmentation, but others show minimal fragmentation. For example, in 2001, Harada et al.[27] shown distinct fragmentation of 1,3-cyclohexadiene (1,3-CHD) and 1,4-cyclohexadiene at 800 nm with a 120 fs pulse width. For 1,3-CHD, the parent ion dominated the mass spectra but there was much less parent ion signal in 1,4-CHD TOF mass spectrum. They concluded that this depends on whether the molecular cation has resonance over-

lapped with the femtosecond laser wavelength (usually the Ti-sapphire fundamental, ~780-820 nm). In 2008, Dantus et al.[47] discussed the fragmentation dependence on the shape and the duration of the laser pulse. They concluded that the Fourier transform-limited pulses yield minimum fragmentation for a given pulse duration based on dozens of the molecules studied, the fragmentation only depends on the averaged pulse duration. They also concluded that above the saturation intensity (I_{sat}, was discussed in Chapter 1), the ion signal in mass spectra is robust and has strong signal-to noise ratio. The ionization is "semi-soft" because it not only produces parent ion but also generates moderate system-specific fragmentation. In the kinetics and flame studies at the ALS and Hefei, PIE curves of known samples are used as "basis functions" to identify the complex isomers mixture quantitatively. In the work presented here, the TOF spectra of known samples is considered as "basis functions", rather than PIE curves.

4.2 Experimental Setup

4.2.1 Apparatus

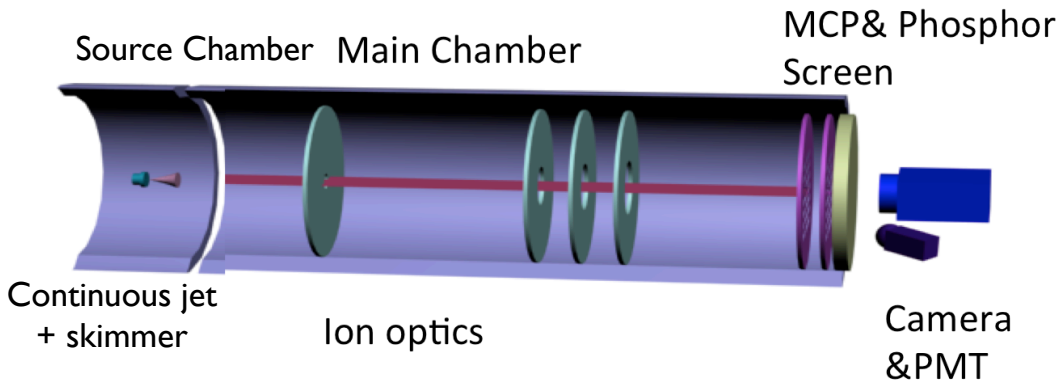

Figure 4.1: The schematic diagram of the experimental setup.

The experiment is carried out in a modified velocity map imaging apparatus[21, 69] but it is only used as a TOF mass spectrometer in these studies (Figure 4.1). Two separate turbo-molecular pumps pump the source and main chambers differentially, and a conical skimmer separates the two chambers. Experimental samples of propyne (Sigma-Aldrich 99+%), allene (Pfaltz&Bauer 96%), 1,3-butadiene (Sigma-Aldrich 99+%), acetone (EMD Millipore 99.5%), propanal (Aldrich 97%) and 1-butyne(Sigma-Aldrich 99%) were used without further purification. A gas sample containing ∼2-5% of the "known" sample or "unknown" mixture was seeded in helium and introduced via a continuous nozzle (20 μm diameter) at a backing pressure of ∼1 bar. The partial pressure of each gas was measured by a capacitance manometer. The uncertainty in the prepared concentration of each gas sample or mixture is estimated to be around 1% of the target value and is neglected in the analysis. The pressure was maintained at 10^{-6} torr and 10^{-7} torr in the source and main chambers (uncorrected ionization gauge readings) with the gas sample flowing. The pressure of the gas sample was controlled by a needle valve to keep the pressure inside the source and main chamber constant for the different gas samples and mixtures, ensuring a constant total number density of the heavy components in the molecular beam. After passing through a skimmer, the molecular beam arrived in the main chamber and was intersected perpendicularly by a laser beam provided by an amplified 800 nm femtosecond Ti:Sapphire laser system(nominally 45 fs, 3 mJ/pulse, 1 kHz KMlabs, Wyvern 1000). After passing through a half-wave plate coupled with a thin film polarizer set at Brewster's angle, the linearly polarized laser beam was focused into the main chamber by 30 cm focal length lens. The power of the laser could thus be smoothly adjusted by rotating the half-wave plate manually. The repeller voltage was maintained at +1400 V, the extractor was maintained at +1230 V, and another lens operated at +1080 V. After passing through a 1 m field free flight tube, the ions were

detected by a dual MCP/P-47 phosphor screen detector of 75 mm diameter. The TOF data was recorded by a PMT fed to a digital oscilloscope where it was averaged and transferred to a computer for additional accumulation, display and storage. Because this is a DC slice imaging apparatus[69], mass resolution has been sacrificed for reduction of chromatic aberration in imaging experiments. Future studies will employ a reflectron for higher mass resolution, but the limited mass resolution does not interfere with our ability to analyze and quantify the samples, as seen below, and may reduce the sensitivity of the data acquisition to electronic jitter.

4.2.2 Detection sensitivity

To discuss the sensitivity of the detection, we need to consider the focal volume effect of the laser beam at first. The laser beam profile is approximated to be a Gaussian beam profile. The Gaussian beam waist radius (minimum spot size ω_0) is estimated to be 30 μm using a 300 mm focal lens. The Rayleigh range (z_R) is indicated as the length of focus and it is given by $z_R = \frac{\pi\omega_0^2}{\lambda}$. It is 3.5 mm along the laser propagation axis. Therefore, the focal shell by the laser beam can be simulated to a concentric cylinder and the volume of the sample (V_i) above the ionization threshold (I_i) can be calculated by the the formula $V_i = 2/9\pi\omega_0^2 z_R (I_f/I_i)^{3/2}$[47] ($I_f$ is the peak intensity of laser beam). For propyne, if the laser peak intensity is 1.9×10^{14}W/cm^2, the calculated volume (V_i) above the saturation intensity ($I_i = I_{sat} \approx 1.1 \times 10^{14} W/cm^2$) is around $5 \times 10^{-8} cm^3$.

For our experiment, the pressure of propyne behind the nozzle is ~13.5 torr. It is obtained by the equation below.

$$P_{propyne} = \frac{P_{chamber}\hat{S}}{2 \times 10^5 \times A(m^2)} \tag{4.1}$$

$P_{chamber}$ is the pressure in the source chamber with gas flow, $\hat{S}$ is the pumping speed and A is the area of the aperture. The laser interaction area is 34.5 cm away from the nozzle ($d = 34.5$ cm). The pressure around the interaction area is calculated by the following equation

$$P_{focal} = P_{propyne}(\frac{x_M}{d})^2 \tag{4.2}$$

where $x_M = 20\ \mu m$ is the nozzle diameter. The propyne pressure of the laser focal area is $5 \times 10^{-8}\ torr$ with the 20 micron diameter nozzle, which corresponds to a number density of $1.5 \times 10^9 cm^{-3}$. I_{sat} has been discussed by Corkum et al. in detail and it is assumed as a value that all the species in the focal volume are ionized as discussed in Chapter 1. Therefore, it is about hundred molecules ionized in the focal volume. The dominant species in the stain steel chamber are H_2, CO and H_2O. The saturation intensities of H_2 and CO are much higher compared with propyne and other samples using in the experiment as well, which are $\sim 10^{17}$ and $10^{19}\ W/cm^2$[72], respectively. Thus, the focal volumes related to H_2 and CO are very small and can be ignored. The main background signal should be from water ions. The background pressure of the laser focal area in the main chamber is $1 \times 10^{-8}\ torr$, so there are less than 10 water molecules ionized in the same area.

In the isomer specific experiment operated by T.Cool et al.[14] at the ALS, the concentration profile of the ions detected was $\tilde{}10^{-9} mol/cm^3$. But for SFI detection, the mole concentration profile of the ions is $\tilde{}10^{-14} mol/cm^3$ assuming the detection efficiency of the detection is around 50%. Compared with ALS experiment, the sensitivity of SFI detection is much greater, although the maximum detection volume is small.

4.3 Results and Discussion

4.3.1 Allene and Propyne

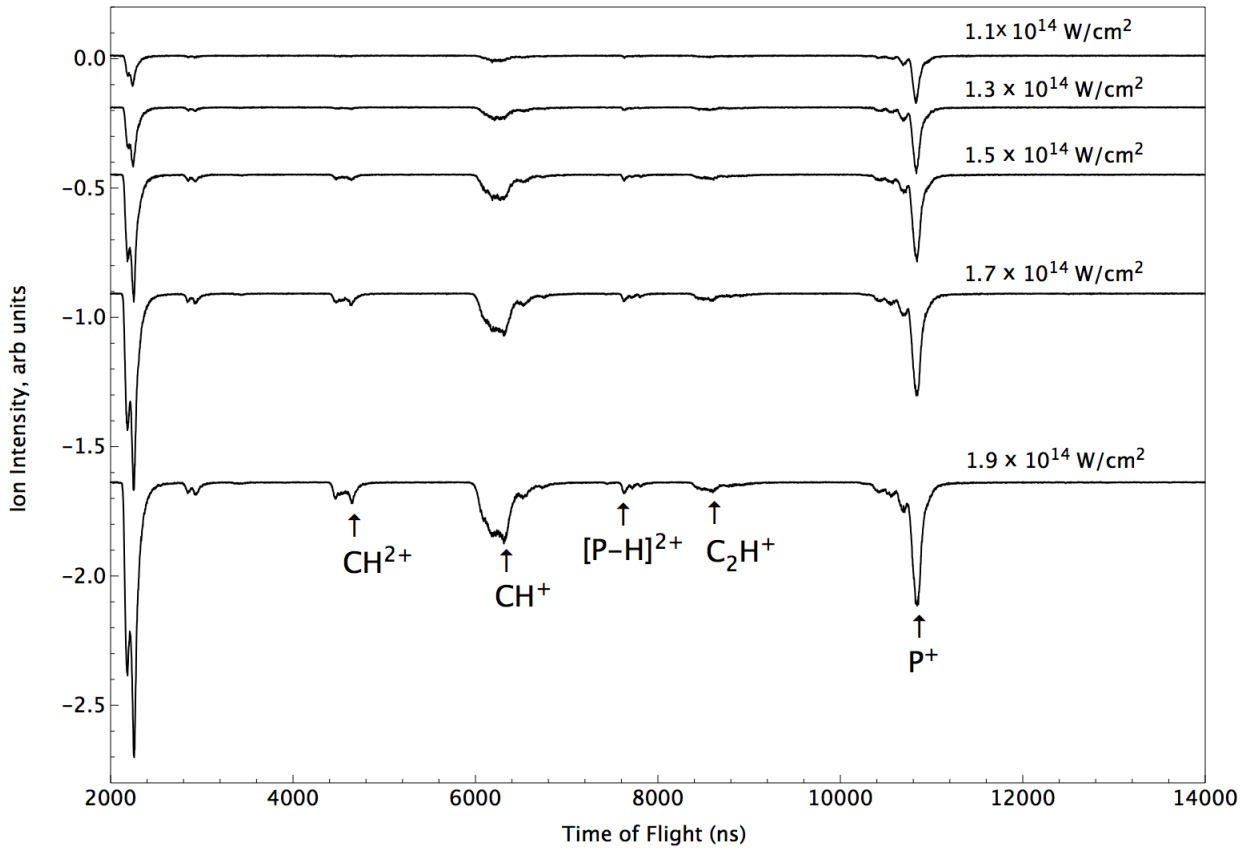

Figure 4.2: Laser intensity dependence of time-of-flight spectra of propyne and obtained by strong field ionization above $1.1 \times 10^{14} W/cm^2$.

We first show the variation in the strong-field ionization mass spectrum with laser intensity. In all spectra presented here, the laser beam is assumed to have a Gaussian intensity profile, and the laser pulse duration is minimized and estimated to be on the order of 70 fs at the interaction region. These assumptions give reasonable values for the saturation intensities for the different detected species as discussed below. The raw TOF spectra of propyne (CH_3CCH) at a range of laser intensities (above $1.1 \times 10^{14}\ W/cm^2$) are shown in Fig. 4.2. The fragmentation of propyne is not

complicated, and the major peaks are assigned in the spectra. The dominant signal is the singly charged parent ion (m/z=40) and methylidene cation (m/z=13). We can also assign the peaks of C_2H^+, $C_3H_3{}^{2+}$ and CH^{2+}. There is also a strong signal at both molecular and atomic hydrogen. The fragmentation of allene is different from propyne and will be discussed later. For both propyne and allene TOF spectra, the magnitude of each peak grows with increasing laser intensity; however, the relative peak intensity is largely independent of laser power in this region, and this is consistent with the observation reported by Dantus and coworkers that it is the laser pulse duration rather than the peak intensity that has the greatest impact on fragmentation, with Fourier transform-limited pulses giving the minimum fragmentation.

The total ion yield and that of the parent ion were then obtained by integrating the TOF spectra of propyne (Fig. 4.2) and allene (not shown). Fig. 4.3 shows the total ion yield of allene and propyne as a function of laser intensity. If strong-field ionization is treated using the barrier suppression ionization model then a plot of the ion intensity versus the logarithm of the laser intensity yields a straight line, and its intercept with the laser intensity axis gives the saturation intensity, I_{sat}. Under these conditions the ionization is saturated within the focal volume, and the growth in the ion yield represents the increase in the effective focal volume with laser power. This gives a rough indication of the ease of ionization, and in general it tracks the ionization energy of the molecule under study. The corresponding plots for allene and propyne are shown in Fig. 4.3: I_{sat} values of 1.08×10^{14} and $1.13\times10^{14} W/cm^2$ were obtained for allene and propyne, respectively. These are in reasonable agreement with the values reported by Cornaggia et al.[18] and Uiterwaal et al.[72] and consistent with the respective ionization energies of 9.69 and 10.32 eV[45]. As discussed by Dantus[47], measurements are more reliable above the I_{sat} because the robust signal results in the high signal-noise ratio and the ionization mechanisms do not change in this region.

All the mass spectra presented here were collected above I_{sat}.

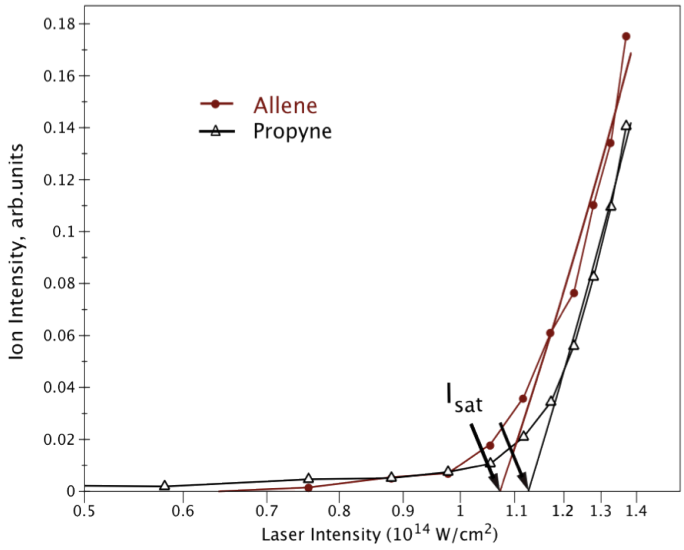

Figure 4.3: Total ion yield of allene and propyne as a function of laser intensity. Saturation intensities (I_{sat}) are obtained by linear regression to the linear regions of the spectra.

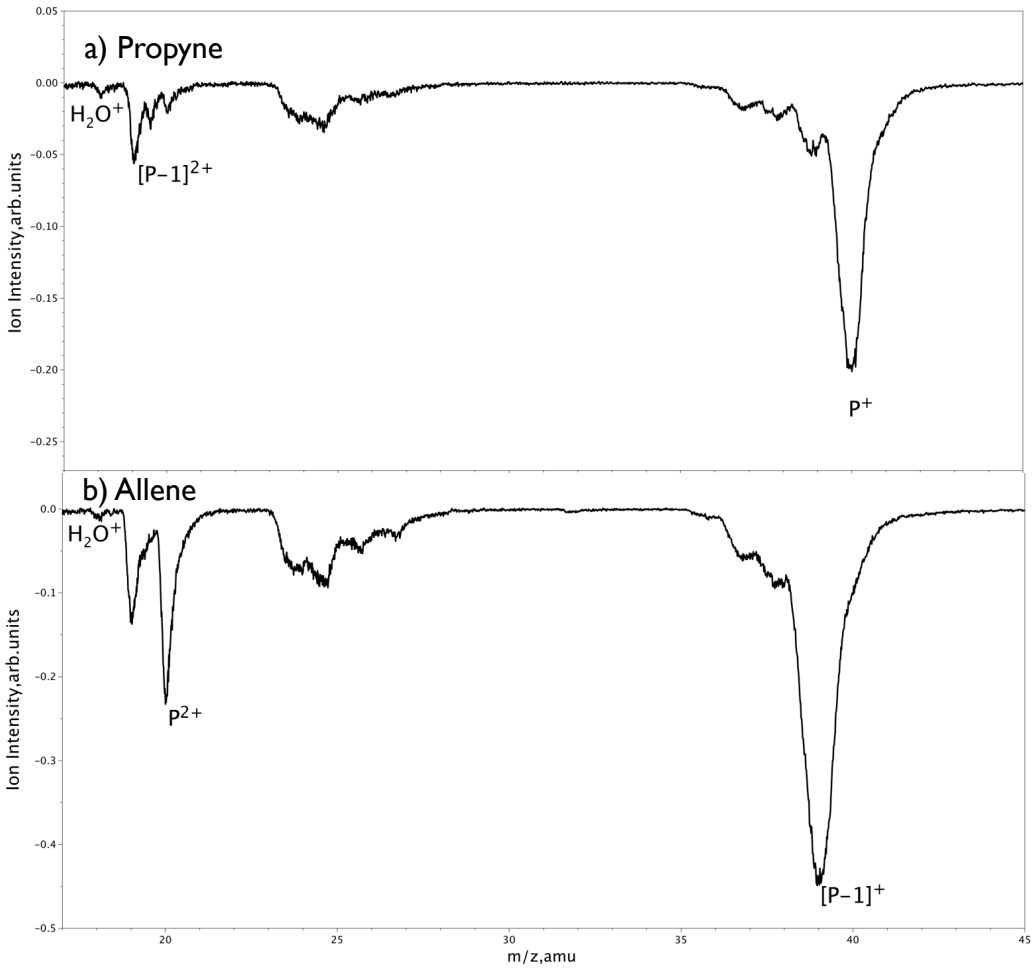

Figure 4.4: Experimental mass spectra produced by strong field ionization of a) propyne, b) allene.

If we compare the mass spectra of allene and propyne measured at a laser intensity of 1.5×10^{14} W/cm^2 (above I_{sat} of both isomers) shown in Fig. 4.4, it is easy to identify the fragmentation differences between them, especially around the parent ion mass range. In each of these spectra, the water peak (m/z=18) is from background in the chamber. For propyne, the peak of the parent ion is seen at mass 40, but allene shows a peak at m/z=39 (parent minus H, ([P-H]+)), dominating the mass spectrum. Allene also has a small peak at m/z=20, double ionization of the parent molecule

(P^{2+}). These distinct peaks dominate the mass spectra for each isomer, so when we examine a mixture of allene and propyne, the presence of both isomers is immediately apparent and their contributions easily quantified. The TOF spectrum of the mixture was carried out at the same laser intensity and the same total concentration as each pure sample. Since each isomer has characteristic fragmentation, its mass spectral "fingerprint" may be used to identify and quantify its contribution to the mixture. The mixture was prepared with 40.4% propyne and 59.6% allene as summarized in Table 4.2. The spectra were recorded with 12,000 laser shots corresponding to ~2 minutes at a laser repetition rate of 1 kHz.

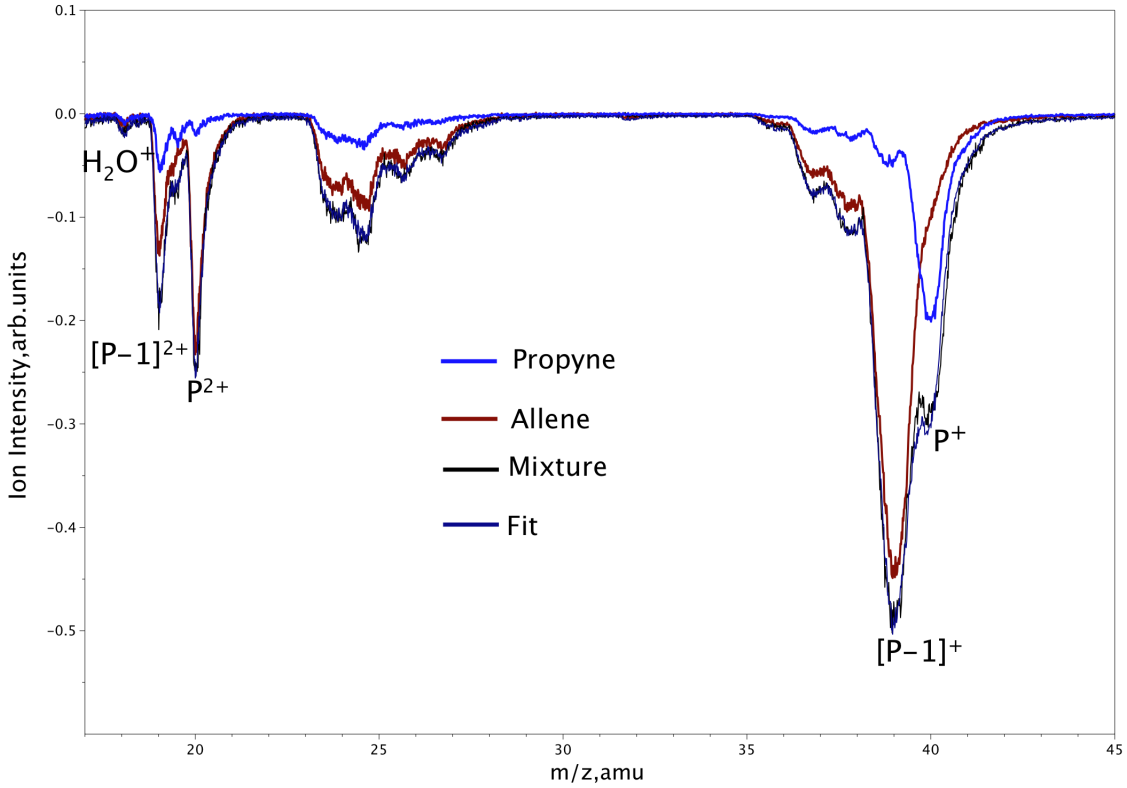

Figure 4.5: Experimental mass spectra by strong field ionization of allene-propyne mixture.

A simple linear regression model (Eq (4.1)) using was used to fit the mixture spectrum to a linear combination of the pure allene and propyne spectra:

$$I_{mix}(t) = x_a I_a(t) + x_p I_p(t) + C \tag{4.3}$$

I_{mix}, I_a and I_p represent the ion intensity in a certain flight time range of interest for the mixture, allene and propyne spectra, respectively. The constant C corresponds to the baseline variation of the oscilloscope. The allene-propyne mixture sample contains 38.9% propyne and 61.1% allene. The results from the fitting in various laser intensities from $1.1 \times 10^{14}\ W/cm^2$ to $1.9 \times 10^{14}\ W/cm^2$ are illustrated Table 4.1. In Fig. 4.5, we illustrated the fitting mass spectra with the mass spectrum obtained from experiment in laser intensity $1.5 \times 10^{14}\ W/cm^2$. The composition of the allene-propyne mixture inferred from the fits agrees quite well with the known concentration. This result shows the promise of isomer-specific detection based on characteristic fragmentation patterns in strong-field ionization.

	Fit Propyne% at various Laser intensity (10^{14}W/cm^2)					
	1.1×10^{14}	1.3×10^{14}	1.5×10^{14}	1.7×10^{14}	1.9×10^{14}	Mean
Propyne%						
38.9	41.1	41.0	40.9	41.5	42.2	41.3(1.0)

Table 4.1: The composition of allene-propyne mixture at various laser intensities.

4.3.2 1-butyne and 1,3-butadiene

The experiments with 1-butyne, 1,3-butadiene and the mixture were operated in the same method.We show the mass spectra of them in Fig. 4.6 at the range of m/z from 17.35 to 60. From the mass spectra, the fragmentation of 1-butyne and 1,3-butadiene are similar to each other. For 1,3-butadiene, it has stronger signal of parent ion than that of 1-butyne. However, in the mass spectra of 1-butyne, there is a stronger peak of $C_3H_3^+$, which represents CH_2CCH^+ or CH_2CC^+(propagyl radical

ion). For this pair of isomers, it is not easy to distinguish them with comparing only the fragmentation of each mass spectra. Because their mass spectra "finger prints" are not that significant and unique, none of them has an unique mass peak from the fragmentation to distinguish from each other. However, if we only want to know the concentration of each isomer in the mixture quantitatively, the linear regression model can also be applied using the pure samples spectrum. This time, we only collect the spectrum in a certain laser intensity ($1.9 \times 10^{14}\ W/cm^2$ for 1,3-butadiene, 1-butyne and the mixture) to avoid any artificial error occurred by manually changing the power. The TOF spectra of pure 1,3-butadiene and 1-butyne were collected in 120 K laser shots, and the averaged spectra was used to fit the mixture recorded in 12000 laser shots. The fitting was repeated 10 times, and the results are shown in Table 4.2.

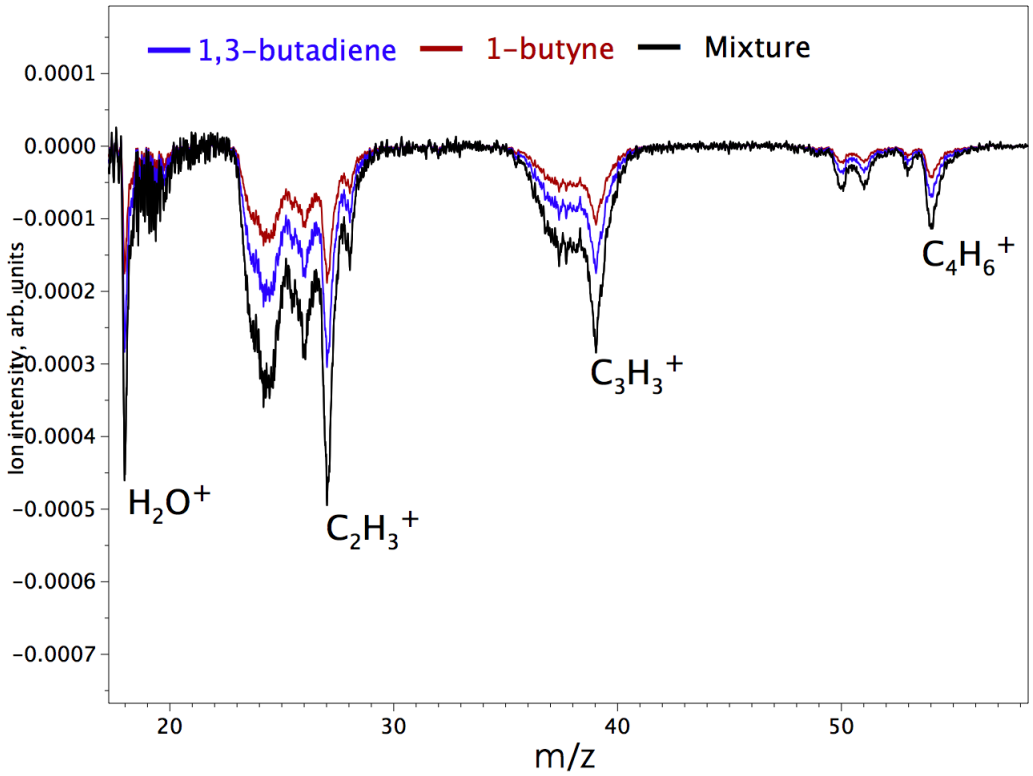

Figure 4.6: Experimental mass spectra by strong field ionization of 1-butyne, 1,3-butadiene and a mixture.

	Allene(%)	Propyne(%)	1,3-Butadiene(%)	1-Butyne(%)	Acetone(%)	Propanal(%)
Mixture 1	40.4	59.6	-	-	-	-
Fit	39.2	60.8	-	-	-	-
Mixture 2	-	-	-	-	31.2	68.8
Fit	-	-	-	-	31.0(2.2)	69.0(2.2)
Mixture 3	35.8	34.0	30.2	-	-	-
Fit	35.0(1.2)	33.7(1.0)	31.3(1.0)	-	-	-
Mixture 4	-	-	59.6	40.4	-	-
Fit	-	-	61.9 (2.0)	38.1(2.0)	-	-

Table 4.2: Summary of all the experimental analyses of mixture composition. The numbers in parentheses denote 2σ uncertainty obtained from a series of independent measurements as described in the text.

4.3.3 Acetone and Propanal

Another pair of isomers, acetone and propanal, is examined with the same method. Fig. 4.7 shows the mass spectra of propanal, acetone and the mixture with the range of m/z=17 and 65. In propanal mass spectrum, the dominate peaks are the parent ion and the peak at m/z=29, which may be the formyl or ethyl radical or both. On the other hand, for acetone, it has peak of acetyl radical and a stronger peak of the parent ion, but there is nearly no peak around m/z=29.

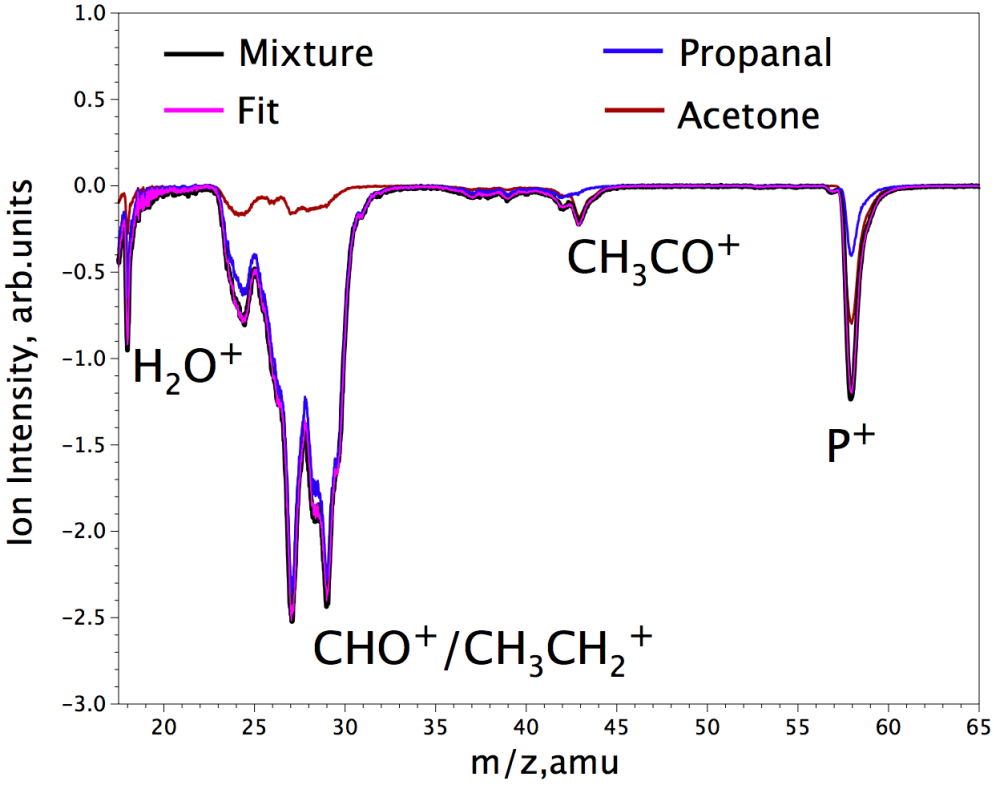

Figure 4.7: Experimental mass spectra by strong field ionization of acetone, propanal and a mixture

Exploiting the characteristic fragmentation of acetone and propanal, we used the spectra of pure acetone and propanal to fit the spectrum of the mixture. The spectra of pure acetone and propyne were collected for 96K laser shots, and the averaged spectrum was used to fit the mixture recorded for 12000 laser shots. The fitting was repeated 9 times, and the results are shown in Table 4.2.

4.3.4 Allene, propyne and 1,3-butadiene

This method to identify the composition of each molecule is not limited to isomers. Fig. 4.8 displays the mass spectra of allene, propyne, 1,3-butadiene and the mixture of them. The fragmentation of allene and propyne was discussed earlier. For 1,3-

butadiene, the parent ion (m/z=54) dominates the spectrum and there is no peaks around m/z=39 and 40. The mixture spectrum has strong peaks at m/z=39 and 40 which indicates the presence of allene and propyne.

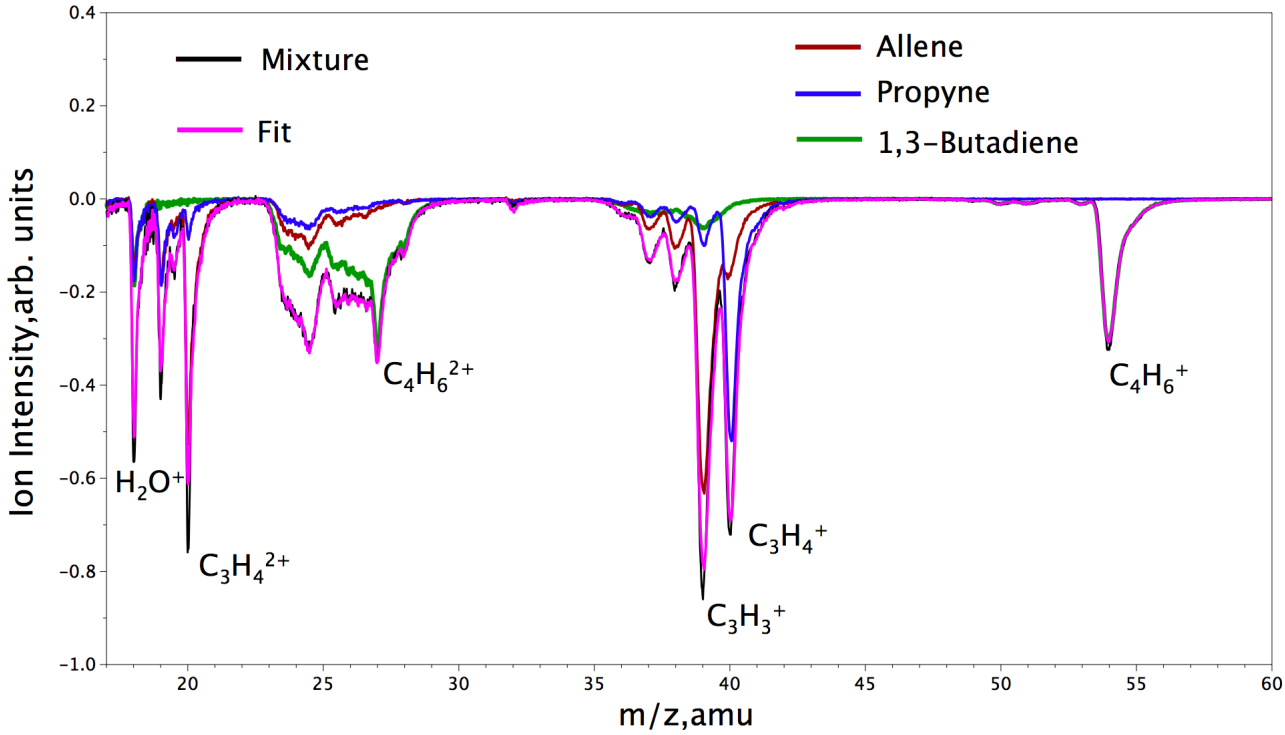

Figure 4.8: Experimental mass spectra by strong field ionization of allene, propyne, 1,3-butadiene and a mixture.

The fitting method is also based on a the linear combination of the mass spectra of each molecule. The mass spectra of allene, propyne and 1,3-butadiene were averaged for 144K laser shots. They were then used to fit the mixture spectrum, which is recorded for 12000 laser shots and averaged 12 times. The fitting result is summarized in Table 4.2.

Strong field ionization is thus considered to be a "semi-soft" ionization compared with electron impact ionization. Electron impact is a powerful and universal method, but it is a "hard" ionization method with little parent ion and huge fragmentation. For allene and propyne, the mass spectra by electron impact[45] are nearly identical

to each other and impossible to use for isomeric composition detection.

The mass spectrum of 1,3-butadiene generated by electron impact shows strong peaks at m/z=39 and 40[45]. This overlaps with the mass spectra of allene and propyne by electron impact and one could not specify the existence of allene and propyne in the mixture on this basis. Compared with electron impact, strong field ionization is a general method that can achieve the selective identification for complex mixtures.

4.3.5 Conclusion

In this chapter, we reported a new method of isomer selection measurement quantitatively by use of nonresonant multiphoton ionization mass spectra. The concentration of each isomer in a complex mixture is determined by the mass spectra of each isomer in the strong field ionization by a femtosecond laser. The results of fitting have a good agreement with known concentration of the prepared sample. The selectivity of this "semi-soft" ionization is more sensitive compared with electron impact ionization. Since the apparatus is designed for DC slice imaging, the mass resolution has been sacrificed for velocity resolution. In the future, a reflectron for higher mass resolution will be employed. The isomer selective detection will be used to explore multichannel reactions in the flame or photodissociation to understand the mechanism of the reaction of polyatomic molecules.

REFERENCES

[1] M V Delone N B Krainov V P Ammosov. Tunnel ionization of complex atoms and of atomic ions in an alternating electromagnetic field. *Sov. Phys. JETP*, 91: 2008, 1986.

[2] S Augst, D D Meyerhofer, D Strickland, and S L Chint. Laser ionization of noble gases by Coulomb-barrier suppression. *J. Opt. Soc. Am. B*, 8(4):858–867, 04 1991.

[3] I Barth and O Smirnova. Nonadiabatic tunneling in circularly polarized laser fields: Physical picture and calculations. *Physical Review A*, 84(6), December 2011.

[4] Noel S Bayliss and Eion G McRae. Solvent Effects in the Spectra of Acetone, Crotonaldehyde, Nitromethane and Nitrobenzene. *The Journal of Physical Chemistry*, 58(11):1006–1011, 1954 1954.

[5] A Becker, L Plaja, P Moreno, M Nurhuda, and F H M Faisal. Total ionization rates and ion yields of atoms at nonperturbative laser intensities. *Physical Review A*, 64(2):023408, 07 2001.

[6] A Bhargava and P R Westmoreland. MBMS analysis of a fuel-lean ethylene flame. *Combustion and Flame*, 115(4):456–467, 1998.

[7] Normand C Blais. Photofragmentation of nitromethane in a molecular beam at 193 nm. *The Journal of Chemical Physics*, 79(4):1723–1731, 08 1983.

[8] David A Blank, Weizhong Sun, Arthur G Suits, Yuan T Lee, Simon W North,

and Gregory E Hall. Primary and secondary processes in the 193 nm photodissociation of vinyl chloride. *J. Chem. Phys.*, 108(13):5414–5425, 04 1998.

[9] M Brouard, R Cireasa, A P Clark, T J Preston, C Vallance, G C Groenenboom, and O S Vasyutinskii. O(3PJ) Alignment from the Photodissociation of SO2 at 193 nm. *Journal of Physical Chemistry A: Molecules, Spectroscopy, Kinetics, Environment and General Theory*, 108(39):7965–7976, 2004 2004.

[10] L J Butler, D Krajnovich, Y T Lee, G S Ondrey, and R Bersohn. The photodissociation of nitromethane at 193 nm. *The Journal of Chemical Physics*, 79(4): 1708–1722, 08 1983.

[11] G Capozza, E Segoloni, F Leonori, G G Volpi, and P Casavecchia. Soft electron impact ionization in crossed molecular beam reactive scattering: The dynamics of the O (3P)+ C2H2 reaction. *J. Chem. Phys.*, 120(10):4557–4560, 2004.

[12] D W Chandler and P L Houston. TwoÄêdimensional imaging of stateÄêselected photodissociation products detected by multiphoton ionization. *The Journal of Chemical Physics*, 87:1445, 1987.

[13] Gen Chen, Wu Yu, Jin Fu, Jun Mo, Zuohua Huang, Jiuzhong Yang, Zhandong Wang, Hanfeng Jin, and Fei Qi. Experimental and modeling study of the effects of adding oxygenated fuels to premixed n-heptane flames. *Combustion and Flame*, 159(7):2324–2335, July 2012.

[14] T A Cool, K Nakajima, T A Mostefaoui, F Qi, A McIlroy, P R Westmoreland, M E Law, L Poisson, D S Peterka, and M Ahmed. Selective detection of isomers with photoionization mass spectrometry for studies of hydrocarbon flame chemistry. *J. Chem. Phys.*, 119(16):8356–8365, October 2003.

[15] T A Cool, A McIlroy, F Qi, P R Westmoreland, L Poisson, D S Peterka, and M Ahmed. Photoionization mass spectrometer for studies of flame chemistry with a synchrotron light source. *Rev.Sci.Instrum.*, 76(9), September 2005.

[16] T A Cool, K Nakajima, C A Taatjes, A McIlroy, P R Westmoreland, M E Law, and A Morel. Studies of a fuel-rich propane flame with photoionization mass spectrometry. *Proceedings of the Combustion Institute*, 30:1681–1688, 2005.

[17] T A Cool, J Wang, K Nakajima, C A Taatjes, and A McIlroy. Photoionization cross sections for reaction intermediates in hydrocarbon combustion. *Int. J. Mass Spectrom.*, 247(1-3):18–27, December 2005.

[18] C Cornaggia and Ph Hering. Nonsequential double ionization of small molecules induced by a femtosecond laser field. *Phys. Rev. A*, 62(2):023403, 07 2000.

[19] Bogdan R Cosofret, Scott M Dylewski, and Paul L Houston. Changes in the Vibrational Population of SO(3-) from the Photodissociation of SO2 between 202 and 207 nm. *Journal of Physical Chemistry A: Molecules, Spectroscopy, Kinetics, Environment and General Theory*, 104(45):10240–10246, 2000 2000.

[20] Michael J S Dewar, James P Ritchie, and Jack Alster. Ground states of molecules. 65. Thermolysis of molecules containing NO2 groups. *The Journal of Organic Chemistry*, 50(7):1031–1036, 1985 1985.

[21] A T J B Eppink and D H Parker. Velocity map imaging of ions and electrons using electrostatic lenses: Application in photoelectron and photofragment ion imaging of molecular oxygen. *Rev.Sci.Instrum.*, 68(9):3477–3484, 1997.

[22] Wayne M Flicker, Oren A Mosher, and Aron Kuppermann. Variable angle

electron-impact excitation of nitromethane. *The Journal of Chemical Physics*, 72(4):2788–2794, 02 1980.

[23] Eleftherios Goulielmakis, Zhi-Heng Loh, Adrian Wirth, Robin Santra, Nina Rohringer, Vladislav S Yakovlev, Sergey Zherebtsov, Thomas Pfeifer, Abdallah M Azzeer, Matthias F Kling, Stephen R Leone, and Ferenc Krausz. Real-time observation of valence electron motion. *Nature*, 466(7307):739–743, 08 2010.

[24] S M Hankin, D M Villeneuve, P B Corkum, and D M Rayner. Intense-field laser ionization rates in atoms and molecules. *Phys. Rev. A*, 64(1):013405, 06 2001.

[25] Nils Hansen, Terrill A Cool, Phillip R Westmoreland, and Katharina Kohse-Hoinghaus. Recent contributions of flame-sampling molecular-beam mass spectrometry to a fundamental understanding of combustion chemistry. *Progress in Energy and Combustion Science*, 35(2):168–191, October 2009.

[26] Nils Hansen, James A Miller, Phillip R Westmoreland, Tina Kasper, Katharina Kohse-Hoinghaus, Juan Wang, and Terrill A Cool. Isomer-specific combustion chemistry in allene and propyne flames. *Combust. Flame*, 156(11):2153–2164, 2009.

[27] H Harada, S Shimizu, T Yatsuhashi, S Sakabe, Y Izawa, and N Nakashima. A key factor in parent and fragment ion formation on irradiation with an intense femtosecond laser pulse. *Chemical Physics Letters*, 342(5-6):563–570, July 2001.

[28] Michael L Hause, Nuradhika Herath, Rongshun Zhu, M C Lin, and Arthur G Suits. Roaming-mediated isomerization in the photodissociation of nitrobenzene. *Nat Chem*, 3(12):932–937, 12 2011.

[29] A J R Heck and D W Chandler. IMAGING TECHNIQUES FOR THE STUDY

OF CHEMICAL-REACTION DYNAMICS. *Annual Review of Physical Chemistry*, 46:335–372, 1995.

[30] Naoki Hemmi and Arthur G Suits. Photodissociation of Oxalyl Chloride at 193 nm Probed via Synchrotron Radiation. *Journal of Physical Chemistry A: Molecules, Spectroscopy, Kinetics, Environment and General Theory*, 101(36): 6633–6637, 1997 1997.

[31] Koichi Honda, Hitoshi Mikuni, and Makoto Takahasi. Photolysis of Nitromethane in Gas Phase at 313 nm. *Bulletin of the Chemical Society of Japan*, 45(12):3534–3541, 1972.

[32] Wen-Fang Hu, Tian-Jing He, Dong-Ming Chen, and Fan-Chen Liu. Theoretical Study of the CH3NO2 Unimolecular Decomposition Potential Energy Surface. *Journal of Physical Chemistry A: Molecules, Spectroscopy, Kinetics, Environment and General Theory*, 106(32):7294–7303, 2002 2002.

[33] Hideto Kanamori, James E Butler, Kentarou Kawaguchi, Chikashi Yamada, and Eizi Hirota. Spin polarization in SO photochemically generated from SO[sub 2]. *The Journal of Chemical Physics*, 83(2):611–615, 07 1985.

[34] T Kasper, P Osswald, U Struckmeier, K Kohse-Hoinghaus, C A Taatjes, J Wang, T A Cool, M E Law, A Morel, and P R Westmoreland. Combustion chemistry of the propanol isomers - investigated by electron ionization and VUV-photoionization molecular-beam mass spectrometry. *Combustion and Flame*, 156(6):1181–1201, June 2009.

[35] Hideki Katagiri, Tokuei Sako, Akiyoshi Hishikawa, Takeki Yazaki, Ken Onda, Kaoru Yamanouchi, and Kouichi Yoshino. Experimental and theoretical exploration of photodissociation of SO2 via the C1B2 state: identification of the

dissociation pathway. *Journal of Molecular Structure*, 413–414(0):589–614, 9 1997.

[36] Hong Lae Kim, M A Wickramaaratchi, Xiaonan Zheng, and G E Hall. Reactions of velocity-aligned atoms probed by Doppler profiles: H+O[sub 2] –> OH+O. *The Journal of Chemical Physics*, 101(3):2033–2050, 08 1994.

[37] Katharina Kohse-Hoinghaus, Patrick Osswald, Ulf Struckmeier, Tina Kasper, Nils Hansen, Craig A Taatjes, Juan Wang, Terrill A Cool, Saugata Gon, and Phillip R Westmoreland. The influence of ethanol addition on premixed fuel-rich propene–oxygen–argon flames. *Proc. Comb. Inst.*, 31(1):1119–1127, January 2007.

[38] C Kosmidis, K W D Ledingham, H S Kilic, T McCanny, R P Singhal, A J Langley, and W Shaikh. On the Fragmentation of Nitrobenzene and Nitrotoluenes Induced by a Femtosecond Laser at 375 nm. *Journal of Physical Chemistry A: Molecules, Spectroscopy, Kinetics, Environment and General Theory*, 101(12): 2264–2270, 1997 1997.

[39] Suk Kyoung Lee, Dave Townsend, Oleg S Vasyutinskii, and Arthur G Suits. O(1D2) orbital orientation in the ultraviolet photodissociation of ozone. *Physical Chemistry Chemical Physics*, 7(8):1650–1656, 2005.

[40] Keldysh L, V. *Sov. Phys. JETP*, 20:1037, 1965.

[41] K Q Lao, E Jensen, P W Kash, and L J Butler. Polarized emission spectroscopy of photodissociating nitromethane at 200 and 218 nm. *The Journal of Chemical Physics*, 93(6):3958–3969, 09 1990.

[42] Wen Li, Steven D Chambreau, Sridhar A Lahankar, and Arthur G Suits.

Megapixel ion imaging with standard video. *Review of Scientific Instruments*, 76(6):063106–063107, 06 2005.

[43] Yuyang Li, Lixia Wei, Zhenyu Tian, Bin Yang, Jing Wang, Taichang Zhang, and Fei Qi. A comprehensive experimental study of low-pressure premixed C-3-oxygenated hydrocarbon flames with tunable synchrotron photoionization. *Combustion and Flame*, 152(3):336–359, February 2008.

[44] Yun Fei Lin, Lu Yan, Suk Kyoung Lee, Thushani Herath, and Wen Li. Orbital alignment in photodissociation probed using strong field ionization. *The Journal of Chemical Physics*, 135(23):234311–234314, 12 2011.

[45] P J Linstrom and W G Mallard, editors. *NIST Chemistry WebBook, NIST Standard Reference Database Number 69*. National Institute of Standards and Technology, Gaithersburg MD, 20899, 2005.

[46] Zhi-Heng Loh, Munira Khalil, Raoul E Correa, Robin Santra, Christian Buth, and Stephen R Leone. Quantum State-Resolved Probing of Strong-Field-Ionized Xenon Atoms Using Femtosecond High-Order Harmonic Transient Absorption Spectroscopy. *Physical Review Letters*, 98(14):143601, 04 2007.

[47] V V Lozovoy, X Zhu, T C Gunaratne, D A Harris, J C Shane, and M Dantus. Control of molecular fragmentation using shaped femtosecond pulses. *Journal of Physical Chemistry A: Molecules, Spectroscopy, Kinetics, Environment and General Theory*, 112(17):3789–3812, May 2008.

[48] Jianqiang Ma, Michael J Wilhelm, Jonathan M Smith, and Hai-Lung Dai. Photolysis (193 nm) of SO2: Nascent Product Energy Distribution Examined through IR Emission. *Journal of Physical Chemistry A: Molecules, Spectroscopy, Kinetics, Environment and General Theory*, 116(1):166–173, 2012 2011.

[49] Michael L McKee. Ab initio study of rearrangements on the nitromethane potential energy surface. *Journal of the American Chemical Society*, 108(19):5784–5792, 1986 1986.

[50] D B Moss, K A Trentelman, and P L Houston. 193 nm photodissociation dynamics of nitromethane. *The Journal of Chemical Physics*, 96(1):237–247, 01 1992.

[51] Saburo Nagakura. Ultra-violet absorption spectra and -electron structures of nitromethane and the nitromethyl anion. *Molecular Physics*, 3(2):152–162, 1960 1960.

[52] Nobuaki Nakashima, Seiji Shimizu, Tomoyuki Yatsuhashi, Shuji Sakabe, and Yasukazu Izawa. Large molecules in high-intensity laser fields. *Journal of Photochemistry and Photobiology C: Photochemistry Reviews*, 1(2):131–143, 12 2000.

[53] Minh Tho Nguyen, Hung Thanh Le, Balázs Hajgató, Tamás Veszprémi, and M C Lin. NitromethaneMethyl Nitrite Rearrangement: A Persistent Discrepancy between Theory and Experiment. *Journal of Physical Chemistry A: Molecules, Spectroscopy, Kinetics, Environment and General Theory*, 107(21):4286–4291, 2003 2003.

[54] Hideo Okabe. Fluorescence quenching of sulfur dioxide by source emission gases. *Analytical Chemistry*, 48(11):1487–1489, 1976 1976.

[55] P Osswald, U Struckmeier, T Kasper, K Kohse-Hoinghaus, J Wang, T A Cool, N Hansen, and P R Westmoreland. Isomer-specific fuel destruction pathways in rich flames of methyl acetate and ethyl formate and consequences for the combustion chemistry of esters. *Journal of Physical Chemistry A: Molecules,*

Spectroscopy, Kinetics, Environment and General Theory, 111(19):4093–4101, May 2007.

[56] Patrick Osswald, Hanna Gueldenberg, Katharina Kohse-Hoeinghaus, Bin Yang, Tao Yuan, and Fei Qi. Combustion of butanol isomers - A detailed molecular beam mass spectrometry investigation of their flame chemistry. *Combustion and Flame*, 158(1):2–15, January 2011.

[57] S Paszyc. Photochemistry of nitroalkanes. *Journal of Photochemistry*, 2(3–4): 183–198, January 1974.

[58] F Qi, R Yang, B Yang, C Q Huang, L X Wei, J Wang, L S Sheng, and Y W Zhang. Isomeric identification of polycyclic aromatic hydrocarbons formed in combustion with tunable vacuum ultraviolet photoionization. *Rev.Sci.Instrum.*, 77(8), August 2006.

[59] Fei Qi. Combustion chemistry probed by synchrotron VUV photoionization mass spectrometry. *Proc. Comb. Inst.*, 34(1):33–63, 2013.

[60] T P Rakitzis, S A Kandel, A J Alexander, Z H Kim, and R N Zare. Photofragment helicity caused by matter-wave interference from multiple dissociative states. *Science*, 281(5381):1346–1349, August 1998.

[61] Paresh C Ray, Michael F Arendt, and Laurie J Butler. Resonance emission spectroscopy of predissociating SO[sub 2] C-tilde(1 [sup 1]B[sub 2]): Coupling with a repulsive [sup 1]A[sub 1] state near 200 nm. *The Journal of Chemical Physics*, 109(13):5221–5230, 10 1998.

[62] John D Savee, Satchin Soorkia, Oliver Welz, Talitha M Selby, Craig A Taatjes,

and David L Osborn. Absolute photoionization cross-section of the propargyl radical. *J. Chem. Phys.*, 136(13), April 2012.

[63] Roberta P Saxon and Megumu Yoshimine. Theoretical study of nitro–nitrite rearrangement of CH3NO2. *Canadian Journal of Chemistry*, 70(2):572–579, 1992 1992.

[64] Wayne Sharfin, Michael Ivanco, and Stephen C Wallace. Quantum beat phenomena in the fluorescence decay of the C-tilde([sup 1]B[sub 2]) state of SO[sub 2]. *The Journal of Chemical Physics*, 76(4):2095–2096, 02 1982.

[65] Weizhong Sun, Keiichi Yokoyama, Jason C Robinson, Arthur G Suits, and Daniel M Neumark. Discrimination of product isomers in the photodissociation of propyne and allene at 193 nm. *J. Chem. Phys.*, 110(9):4363–4368, 03 1999.

[66] C A Taatjes, N Hansen, A McIlroy, J A Miller, J P Senosiain, S J Klippenstein, F Qi, L Sheng, Y Zhang, and T A Cool. Enols are common intermediates in hydrocarbon oxidation. *Science*, 308(5730):1887–1889, 2005.

[67] W D Taylor, T D Allston, M J Moscato, G B Fazekas, R Kozlowski, and G A Takacs. Atmospheric photodissociation lifetimes for nitromethane, methyl nitrite, and methyl nitrate. *International Journal of Chemical Kinetics*, 12(4): 231–240, 1980.

[68] Zhenyu Tian, Lidong Zhang, Yuyang Li, Tao Yuan, and Fei Qi. An experimental and kinetic modeling study of a premixed nitromethane flame at low pressure. *Proc. Comb. Inst.*, 32:311–318, 2009.

[69] D Townsend, M P Minitti, and A G Suits. Direct current slice imaging. *Rev.Sci.Instrum.*, 74(4):2530–2539, 2003.

[70] Adam J Trevitt, Fabien Goulay, Giovanni Meloni, David L Osborn, Craig A Taatjes, and Stephen R Leone. Isomer-specific product detection of CN radical reactions with ethene and propene by tunable VUV photoionization mass spectrometry. *Int. J. Mass Spectrom.*, 280(1-3):113–118, 2009.

[71] E B Tulenko and B A Zon. On the tunneling ionization of atoms in the presence of a circularly polarized laser field. *Laser Physics*, 13(4):450–451, 2003.

[72] C J G J Uiterwaal, C R Gebhardt, H Schröder, and K L Kompa. Predicting intense-field photoionization of atoms and molecules from their linear photoabsorption spectra in the ionization continuum. *The European Physical Journal D - Atomic, Molecular, Optical and Plasma Physics*, 30(3):379–392, 2004 2004.

[73] Hajime Watanabe, Soji Tsuchiya, and Seiichiro Koda. Quantum beats in the fluorescence of jet-cooled sulfur dioxide(A 1A2) under a weak magnetic field. *The Journal of Physical Chemistry*, 87(6):906–908, 1983 1983.

[74] Christian Weickhardt and Karen Tönnies. Short pulse laser mass spectrometry of nitrotoluenes: ionization and fragmentation behavior. *Rapid Communications in Mass Spectrometry*, 16(5):442–446, 2002.

[75] A M Wodtke, E J Hintsa, and Yuan T Lee. Infrared multiphoton dissociation of three nitroalkanes. *The Journal of Physical Chemistry*, 90(16):3549–3558, 1986 1986.

[76] Z Xu, B Koplitz, and C Wittig. Velocity-aligned Doppler spectroscopy. *The Journal of Chemical Physics*, 90(5):2692–2702, 03 1989.

[77] B Yang, C Q Huang, L X Wei, J Wang, L S Sheng, Y W Zhang, F Qi, W X Zheng, and W K Li. Identification of isomeric C5H3 and C5H5 free radicals in flame with tunable synchrotron photoionization. *Chemical Physics Letters*, 423 (4-6):321–326, June 2006.

[78] L Young, D A Arms, E M Dufresne, R W Dunford, D L Ederer, C Höhr, E P Kanter, B Krässig, E C Landahl, E R Peterson, J Rudati, R Santra, and S H Southworth. X-Ray Microprobe of Orbital Alignment in Strong-Field Ionized Atoms. *Physical Review Letters*, 97(8):083601, 08 2006.

[79] R S Zhu and M C Lin. CH3NO2 decomposition/isomerization mechanism and product branching ratios: An ab initio chemical kinetic study. *Chemical Physics Letters*, 478(1–3):11–16, 8 2009.

ABSTRACT
FUNDAMENTAL STUDIES AND APPLICATIONS OF STRONG FIELD IONIZATION

by

Lu Yan

August 2013

Advisor: Prof. Arthur G. Suits

Major: Chemistry (Physical)

Degree: Doctor of Philosophy

In an intense laser field, atoms and molecules experience tunneling ionization directly to the continuum. We used this method to study several aspects and applications of strong field ionization (SFI) in atoms and molecules. One study used SFI to probe the photofragments produced by photodissociation using DC sliced imaging. The photodissociation mechanism of two polyatomic molecules (sulfur dioxide and nitromethane) were investigated. In a second study, we show the strong field ionization rate depends on the sign of the magnetic number distribution. We detect the signal of sequential double ionization of argon dications by a pump-probe method to investigate the ionization rate sensitivity to circularly polarized light. In a third study, we also found that the modest fragmentation that accompanies strong field ionization may be used to identify isomers and molecules in a complex mixture based on their mass spectral "finger print". The experiments were carried out in a DC sliced imaging apparatus. For the isomer selective detection experiment, the machine was used simply as a time-of-flight mass spectrometer. The mass spectrum of each isomer was used as "basis function" to characterize the complex mixtures quantitatively.

AUTOBIOGRAPHICAL STATEMENT

Lu Yan

Education:

Aug 2013 Ph.D., Chemistry (*anticipated*), Wayne State University.

Jul 2008 B.S., Physical Chemistry, University of Science and Technology of China.

Recent Publications:

1. S.K. Lee, Y.F. Lin, *L. Yan*, W. Li. "Laser-Induced Low Energy Electron Diffraction in Aligned Molecules" J. Phys. Chem. A 2012, 116, 1950
2. Y.F. Lin, *L. Yan*, S.K. Lee, T. Hearth, W. Li, "Orbital alignment in photodissociation probed using strong field ionization" J. Chem. Phys. 2011, 135, 234311
3. T. Herath, *L. Yan*, S. K. Lee, W. Li, "Strong field ionization depends on the sign of the magnetic quantum number" Phys. Rev. Lett. 2012,109, 043004
4. *L. Yan*, F. Cudry, W. Li, A. G. Suits. "Isomer-specific mass spectrometric detection via "semi-soft" strong-field ionization", J. Phys. Chem. A, in press.